JGR Solid Earth

RESEARCH ARTICLE
10.1029/2019JB018423

Key Points:
- Crustal regions in Southern California with similar seismic velocity profiles are mapped by applying cluster analysis to a tomographic model
- Regions correspond to major physiographic provinces and geologic areas with known tectonic affinities
- Region boundaries are typically narrow, high-angle structures that separate regions with different crustal compositions and tectonic histories

Supporting Information:
- Supporting Information S1

Correspondence to:
T. H. Jordan,
tjordan@usc.edu

Citation:
Eymold, W. K., & Jordan, T. H. (2019). Tectonic regionalization of the Southern California crust from tomographic cluster analysis. *Journal of Geophysical Research: Solid Earth*, *124*, 11,840–11,865. https://doi.org/10.1029/2019JB018423

Received 23 JUL 2019
Accepted 31 OCT 2019
Accepted article online 11 NOV 2019
Published online 29 NOV 2019

©2019. The Authors.
This is an open access article under the terms of the Creative Commons Attribution License, which permits use, distribution and reproduction in any medium, provided the original work is properly cited.

Tectonic Regionalization of the Southern California Crust From Tomographic Cluster Analysis

William K. Eymold[1] and Thomas H. Jordan[2]

[1]School of Earth Sciences, The Ohio State University, Columbus, OH, USA, [2]Department of Earth Sciences, University of Southern California, Los Angeles, CA, U.S.A

Abstract We map crustal regions in Southern California that have similar depth variations in seismic velocities by applying cluster analysis to 1.5 million *P* and *S* velocity profiles from the three-dimensional tomographic model CVM-S4.26. We use a *K*-means algorithm to partition the profiles into *K* sets that minimize the inter-cluster variance. The regionalizations for $K \leq 10$ generate a coherent sequence of structural refinements: each increment of *K* introduces a new region typically by partitioning a larger region into two smaller regions or by occupying a transition zone between two regions. The results for $K \leq 7$ are insensitive to initialization and trimming of the model periphery; nearly identical results are obtained if the *P* and *S* velocity profiles are treated separately or jointly. The regions for $K = 7$ can be associated with major physiographic provinces and geologic areas with recognized tectonic affinities, including the Continental Borderland, Great Valley, Salton Trough, and Mojave Desert. The regionalization splits the Sierra Nevada and Peninsular Range batholiths into the western and eastern zones consistent with geological, geochemical, and potential-field mapping. Three of the regions define a geographic domain comprising almost all of the upper crust derived from continental lithosphere. Well-resolved regional boundaries coincide with major faults, topographic fronts, and/or geochemical transitions mapped at the surface. The consistent alignment of these surface features with deeper transitions in the crustal velocity profiles indicates that regional boundaries are typically narrow, high-angle structures separating regions with characteristic crustal columns that reflect different compositions and tectonic histories.

1. Introduction

The concept of tectonic regionalization is predicated on the notion that plate-tectonic processes produce lithospheric structures that are vertically correlated, regionally coherent, and recognizable from the surface. Lithosphere can be readily separated into regions of thicker continental crust and thinner oceanic crust, and the continents can be further regionalized into shields, platforms, and orogenic belts with distinguishable structural features (e.g., Chen et al., 2018; Jordan, 1981; Mooney et al., 1998). But how useful is the concept of tectonic regionalization at smaller scales?

We address this question by conducting a regionalization analysis of crustal structure in Southern California. Surface mapping (California Geological Survey, 2010; Jennings et al., 1977), in combination with studies of fault offsets, geodetic deformation monitoring, and other kinematic constraints, has taught us a lot about the tectonic assembly and disruption of its distinctive geologic units (Chapman, 2017; Chapman et al., 2012, 2016; Ducea et al., 2009; Jacobson et al., 2011; Saleeby, 2003; Sharman et al., 2015). Yet much remains to be learned about the tectonic relationships between surface geology and deeper crustal features. The crustal structure of Southern California is exceptionally heterogeneous, reflecting a long history of deformation that has juxtaposed crustal terranes of different composition and age, creating deep sedimentary basins flanked by steep mountain ranges (Atwater, 1970; McQuarrie & Wernicke, 2005; Whitmeyer & Karlstrom, 2007). In this study, we map crustal regions in Southern California that have similar depth variations in seismic velocities by a cluster analysis of velocity profiles from a three-dimensional (3D) tomographic model.

The application of seismic tomography to the rich datasets of the Southern California Seismic Network (SCSN) has produced 3D crustal models of increasing accuracy and spatial resolution (Hauksson, 2000; Chen et al., 2007; Lin et al., 2010; Tape et al., 2010; Allam & Ben-Zion, 2012; Lee, Chen, Jordan, Maechling et al., 2014; Zigone et al., 2015). This imaging has been augmented by high-resolution, active-

source experiments (Fuis et al., 2017; Lutter et al., 1999, 2004), as well as by systematic efforts to assimilate exploration and well-log information into the community velocity models (CVMs) of the Southern California Earthquake Center (SCEC) (Kohler et al., 2003; Magistrale et al., 2000; Shaw et al., 2015; Süss & Shaw, 2003).

Here we regionalize the 3D velocity structure of Southern California according to similarities in the profiles of P-wave velocity $\alpha(z)$ and S-wave velocity $\beta(z)$ at depths from $z = 0$ to 50 km. The α and β profiles were extracted from a fifth-generation SCEC model, CVM-S4.26 (Lee, Chen, Jordan, Maechling, et al., 2014), derived by full-3D waveform tomography (F3DT). The tomographic inversion process was initialized using a fourth-generation model, CVM-S4 (Kohler et al., 2003), and involved 26 linearized iterations that perturbed the two Lamé parameters of an isotropic model to fit a large set of earthquake waveforms and ambient-field correlagrams. Interspersed with these structural iterations were inversions that used the 3D structure to refine the earthquake source mechanisms and locations, which increased the accuracy of the tomography (Lee, Chen, Jordan, Maechling, et al., 2014). CVM-S4.26 provides good fits to waveforms of earthquakes recorded after the model was finalized (Lee, Chen, & Jordan, 2014; Taborda et al., 2016; Lee & Chen, 2016). Moreover, it reproduces many crustal features first identified by surface mapping and active-source imaging, such as the geometry of major sedimentary basins (Lee, Chen, & Jordan, 2014, Lee, Chen, Jordan, Maechling, et al., 2014; Lee & Chen, 2016) and the localized contrasts across faults that bound crustal blocks of different seismic velocities (Lee & Chen, 2017). Section 2 describes CVM-S4.26 in more detail.

We partition the set of 1.52 million velocity profiles from CVM-S4.26 into K distinct regions using the K-means clustering algorithm (MacQueen, 1967; Lloyd, 1982; Arthur & Vassilvitskii, 2007). Lekić and Romanowicz (2011a, 2011b) have applied the K-means algorithm to the problem of mantle regionalization; our approach is similar, differing primarily in geographic scale and degree of geologic refinement. The algorithm iteratively categorizes the profiles into a specified number of clusters that minimize the total squared difference between the regionalized sets of profiles and their corresponding centroids. In Section 3, we show that the α and β profiles, treated separately, yield similar regionalizations for $K \leq 7$, motivating us to use the concatenated profiles $\gamma = \{\alpha, \beta\}$ to fix the clusters. We highlight the γ regionalization for $K = 7$ as an especially informative result.

Section 4 compares the regional properties of the upper, middle, and lower crust and investigates vertical correlations in crustal properties using a simple isostatic model. In Section 5, we show that the regions identified by tomography can be associated with recognized physiographic and geologic provinces; moreover, their boundaries often coincide with major faults, topographic discontinuities, and geochemical transitions unknown to the tomographic model except as their manifestations in the seismic velocities. From these correlations, we argue that regional boundaries are typically localized, high-angle structures that separate crustal regions of distinctive compositions and tectonic histories.

2. Description of the tomographic model

The CVM-S4.26 study area covers Southern California and peripheral portions of Arizona, Nevada, and Baja California, extending from San Simeon on the Central Coast southeastward to the Colorado River Delta (Figure 1a). CVM-S4.26 is a digital model of isotropic seismic velocities comprising $992 \times 1{,}536$ geographic nodes spaced at 500-m intervals over an area of 380,928 km^2. We express the latitude λ_n and longitude φ_n of the nth geographic node as $\mathbf{x}_n \equiv (\lambda_n, \varphi_n)$ and represent the velocity profiles at this location by two profile vectors, $\boldsymbol{\alpha}_n$ and $\boldsymbol{\beta}_n$. Each profile contains velocities $\alpha(\mathbf{x}_n, z)$ or $\beta(\mathbf{x}_n, z)$ at 100 discrete depths z spaced at 500-m increments from the surface ($z = 0$ km) to the base of the model ($z = 49.5$ km). For any value of β and any point $\mathbf{x}_n$ within the model area, we define z_β to be the smallest depth where the shear velocity profile exceeds β. Thus, $z_{2.5}(\mathbf{x}_n)$ maps the shallowest depth to the isovelocity surface for $\beta = 2.5$ km/s, which has been used as a proxy for basin depth in ground motion prediction equations (e.g., Campbell & Bozorgnia, 2008, 2014). The $z_{2.5}$ surface for CVM-S4.26 is given in Fig. 1d of Lee and Chen (2016).

2.1. Features of CVM-S4.26

The map of $\beta(\mathbf{x}_n, z)$ at $z = 2$ km (Figure 1a) shows the major sedimentary basins as features of low shear velocity ($\beta < 2.5$, in warm colors). The San Joaquin Basin of the Great Valley is the deepest with $z_{2.5} \approx 8$ km. Also prominent are the Salton Trough and the basins of Santa Maria, Ventura, and Los Angeles. A number of the

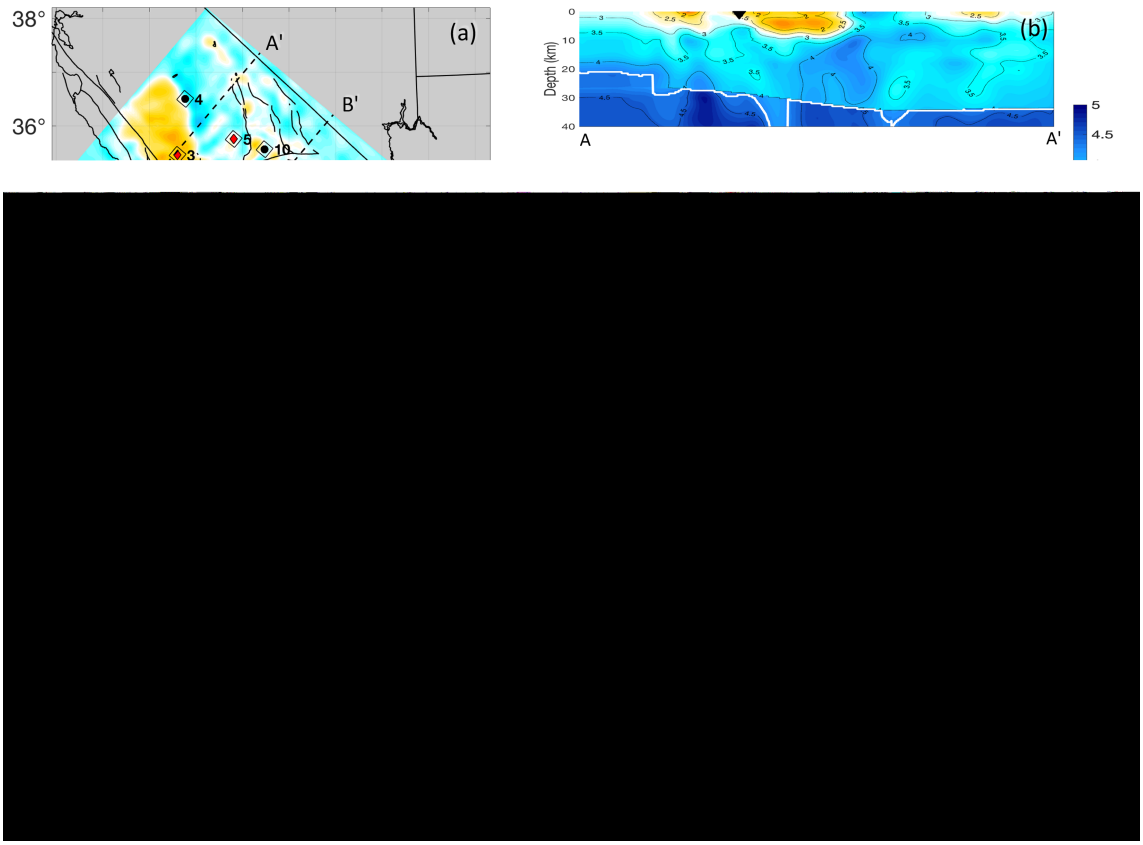

Figure 1. (a) Map of the study area showing the *S*-wave velocity β of CVM-S4.26 at 2-km depth. Fault traces are modified from Jennings et al. (1977). Numbered diamonds mark the locations of the profiles in the bottom panels; those in red were used in the supervised clustering (Figure S6). **(b)-(d)** Cross sections through CVM-S4.26 showing β to a depth of 40 km along the profiles marked on the map; vertical exaggeration 2.4:1. White lines are the 4.3-km/s contours that demarcate the first depth to mantle velocities, which we take to be the nominal location of the M-discontinuity. Triangles mark the surface trace of the San Andreas Fault. **(e)-(g)** β profiles at points marked by numbers on the map in panel (a). The depth to the M-discontinuity is defined as the shallowest depths where the shear velocity reaches 4.3 km/s (dashed-dotted lines). Boundaries between crustal layers and between lower crust and mantle (horizontal dashed lines) are average depths for the study area, picked from gradients in the mean velocity profiles (dashed black profiles).

smaller, shallower basins are well represented in the model, such as those of the Indian Wells, Antelope, and San Fernando valleys (Lee & Chen, 2016).

Cross-sections through the model taken approximately perpendicular to the San Andreas fault system (Figures 1b,c,d) reveal regions of high velocity ($\beta \geq 4$ km/s) at depths near 10 km, many beneath the deeper sedimentary basins. Most of these structures have been recognized in 2D-refraction studies, such as the high-velocity anomaly under the San Gabriel Basin, imaged by the first Los Angeles Regional Seismic Experiment, LARSE-I (Lutter et al., 1999), and beneath the Antelope Valley, imaged by LARSE-II (Lutter et al., 2004). Almost all of the major features appear in one or more of the earlier tomography models (Chen et al., 2007; Hauksson, 2000; Lin et al., 2010; Tape et al., 2010).

The particularly strong positive anomaly on cross-section A-A′ is associated with the Great Valley ophiolite complex accreted to the western edge of the active continental margin in the Mesozoic (Godfrey et al., 1997; Godfrey & Klemperer, 1998). The cross-section shows that the high-velocity anomaly has an eastern boundary at the edge of the batholith and widens with depth as the top of the zone dips under the San Joaquin Valley. The shallow (~10°) dip of this upper interface in CVM-S4.26 is consistent with that inferred from refraction studies and potential-field modeling (Fliedner et al., 2000; Godfrey & Klemperer, 1998; Kaban & Mooney, 2001). This feature is also well-expressed in the tomographic model of Lin et al. (2010).

Shear velocity profiles at 15 selected geographic points, grouped by closest cross-section, are plotted in Figures 1e-g. Each profile was obtained by averaging the 2,601 profiles in a 25-km × 25-km square

$$\boldsymbol{\gamma}_n = \left[\frac{\boldsymbol{\alpha}_n/\sqrt{3}}{\boldsymbol{\beta}_n}\right]. \tag{2}$$

The factor of $\sqrt{3}$ balances the weighting of profile differences according to a Poisson-solid scaling of the two seismic velocities. The mean profiles of the kth cluster, the cluster centroids, are

$$\overline{\boldsymbol{\alpha}}^{(k)} = \frac{1}{N_k}\sum_{\mathbf{x}_n\in\mathbf{X}_k}\boldsymbol{\alpha}_n, \quad \overline{\boldsymbol{\beta}}^{(k)} = \frac{1}{N_k}\sum_{\mathbf{x}_n\in\mathbf{X}_k}\boldsymbol{\beta}_n, \quad \overline{\boldsymbol{\gamma}}^{(k)} = \left[\frac{\overline{\boldsymbol{\alpha}}^{(k)}/\sqrt{3}}{\overline{\boldsymbol{\beta}}^{(k)}}\right]. \tag{3}$$

The profile variations about these means are

$$\Delta\boldsymbol{\alpha}_n^{(k)} = \boldsymbol{\alpha}_n - \overline{\boldsymbol{\alpha}}^{(k)}, \quad \Delta\boldsymbol{\beta}_n^{(k)} = \boldsymbol{\beta}_n - \overline{\boldsymbol{\beta}}^{(k)}, \quad \Delta\boldsymbol{\gamma}_n^{(k)} = \boldsymbol{\gamma}_n - \overline{\boldsymbol{\gamma}}^{(k)}. \tag{4}$$

In this notation, $\overline{\boldsymbol{\alpha}}^{(\mathrm{T})}$, $\overline{\boldsymbol{\beta}}^{(\mathrm{T})}$, and $\overline{\boldsymbol{\gamma}}^{(\mathrm{T})}$ are the mean profiles averaged over the entire model region $\mathbf{X}_{\mathrm{T}}$. $\overline{\boldsymbol{\beta}}^{(\mathrm{T})}$ is plotted as a dashed line in Figures 1e-g.

3.2. Algorithm

We perform a partitional clustering analysis with the K-means function built into MATLAB®, which is based on the K-means++ algorithm of Arthur and Vassilvitskii (2007). At each step in this iterative procedure, a candidate profile is assigned to the cluster whose mean is closest to the candidate. We measure this closeness by the Euclidean distance,

$$\left\|\Delta\boldsymbol{\gamma}_n^{(k)}\right\| = \left(\sum_z\left[\gamma(\mathbf{x}_n,z) - \overline{\gamma}^{(k)}(\mathbf{x}_n,z)\right]^2\right)^{1/2}. \tag{6}$$

In K-means analysis of the γ profiles, the location $\mathbf{x}_n$ is assigned to the cluster $\mathbf{X}_k$ if k is the cluster index that minimizes $\left\|\Delta\boldsymbol{\gamma}_n^{(k)}\right\|$; i.e.,

$$k_n^{(\gamma)} = \arg\min_{1\le k'\le K}\left\|\Delta\boldsymbol{\gamma}_n^{(k')}\right\|. \tag{7}$$

The clustering can either be supervised or unsupervised. In the supervised case, we specify initial values of the K cluster centroids. In unsupervised clustering, the K-means++ algorithm initializes the centroids sequentially, spreading them out by choosing the kth centroid from profiles assigned probabilities according to the squared distance from the $(k-1)$ previously chosen centroids. At each step, each profile is assigned to its closest centroid, and, after all assignments are made, the centroid for each k is recomputed. This procedure is iterated to convergence. In the case of unsupervised learning, we checked that the resulting minimum was global rather than local by running a number (10-100) of independently seeded iterations. For $K \le 10$, most converged to the same minimum of the Euclidean objective function. The γ regionalization of order K is the final set of clusters resulting from this procedure, $RK_\gamma \equiv \left\{\mathbf{X}_k^{(\gamma)} : k = 1,\ldots,K\right\}$. Iterative minimizations of $\left\|\Delta\boldsymbol{\alpha}_n^{(k)}\right\|$ and $\left\|\Delta\boldsymbol{\beta}_n^{(k)}\right\|$ produce regionalizations RK_α and RK_β that generally differ from RK_γ.

3.3. Results

The three types of regionalization, RK_α, RK_β, and RK_γ, were computed from CVM-S4.26 for K up to 10. The maps and centroid profiles for RK_α and RK_β are plotted for K = 3-10 in the Supplementary Information (S.I.). The RK_γ regionalizations, which equally weight the α and β profiles, are displayed for K = 4-6 in Figure 5.

A simple measure of the efficacy of the cluster separation is variance reduction. The summed variance of a concatenated profile $\boldsymbol{\gamma}_n$ about the mean profile $\overline{\boldsymbol{\gamma}}^{(k)}$ is $\left\|\Delta\boldsymbol{\gamma}_n^{(k)}\right\|^2$. We define $\delta_n^{(k)}$ to be the membership indicator that assigns the nth profile to the kth region:

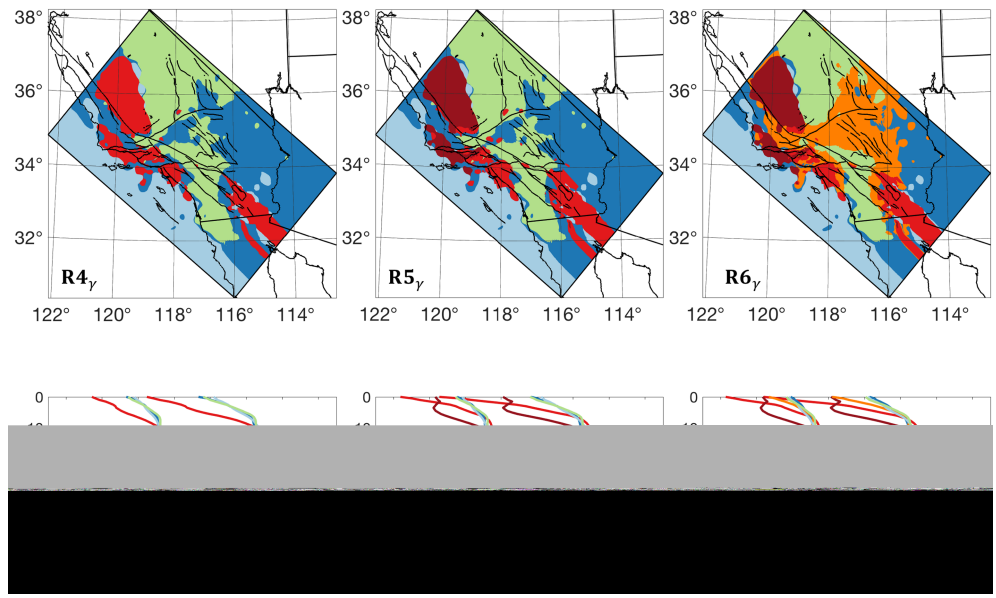

Figure 5. RK_γ regionalizations for K = 4-6. The clusters are identified as colored regions on the maps (top panels). The centroid profiles are plotted as functions of depth in corresponding colors (bottom panels).

$$\delta_n^{(k)} = \begin{cases} 1 \text{ if } \mathbf{x}_n \in \mathbf{X}_k \\ 0 \text{ if } \mathbf{x}_n \notin \mathbf{X}_k \end{cases}. \tag{8}$$

Then, the summed variance over the K regions is

$$V_K = \sum_{n=1}^{N_T} \sum_{k=1}^{K} \delta_n^{(k)} \left\| \Delta \boldsymbol{\gamma}_n^{(k)} \right\|^2. \tag{9}$$

Equation (9) is the objective function minimized by the K-means++ algorithm. Figure 6 plots the total variance for K = 1-10, normalized by the total (unregionalized) variance V_1. The $R3_\gamma$ regionalization reduces the variance by 42%. The reduction increases to 61% for K = 7 but flattens off thereafter, reaching only 66% for K = 10. RK_α and RK_β show similar curves, although the variance reduction of the latter is somewhat smaller, about 64% at K = 10.

3.4. $R7_\gamma$ regionalization

One of the most informative results is $R7_\gamma$, the K-means regionalization of concatenated profiles for K = 7. Each of the seven regions can be associated with a recognized physiographic province (Table 1). These associations typify the regions and provide mnemonically useful regional labels (Figure 7). The $R7_\gamma$ centroid profiles, $\overline{\alpha}^{(k)}(z)$ and $\overline{\beta}^{(k)}(z)$, show correlated regional features (Figure 8) that are further described in §4.1.

The associations among sedimentary basins and among plutonic provinces are geologically coherent. The regions comprise widely separated areas, some of which are physiographic provinces in their own right. The region associated with the Salton Trough, ST, also includes the Los Angeles basins, whereas GV, associated with the Great Valley, also includes the Santa Maria and Santa Barbara basins. The region associated with the Sierra Nevada, SN, includes the

Figure 6. Total residual variance fraction V_K/V_1 as a function of K for the three types of K-means regionalizations.

Table 1
Association of $R7_\gamma$ regions with physiographic provinces

Region #	Label	Map Color	Area (km^2)	Main Province	Other Provinces
1	CB	light blue	79,242	Continental Borderland	none
2	GV	purple	29,857	Great Valley	Santa Maria & Santa Barbara Basins
3	SN	light green	51,767	Sierra Nevada	C. Transverse Ranges
4	PT	dark blue	82,807	Proterozoic Terranes	C. Coast Ranges
5	PR	dark green	31,505	Peninsular Ranges	W. Sierra Nevada
6	ST	red	29,546	Salton Trough	Los Angeles & Ventura Basins
7	MD	orange	76,204	Mojave Desert	W. Transverse & S. Coast Ranges

eastern Transverse Ranges, whereas PR, associated with the Peninsular Ranges, includes the western Sierra Nevada. The SN-PR boundaries on the west side of the Sierra Nevada and the northeast side of the Peninsular Ranges approximate the previously recognized division of the batholiths into eastern and western zones (Chapman et al., 2012, 2016; Gromet & Silver, 1987; Jiang & Lee, 2017; Kimbrough et al., 2015; Sharman et al., 2015). The MD region, which includes most of the Mojave Desert but also southern parts of the Coast Ranges, becomes more consolidated if the right-lateral displacement across the San Andreas Fault is restored. The region comprising most of the Continental Borderland, CB, is almost exclusively the off-shore area of attenuated crustal thickness, including only a few insignificant bubble-like areas in the continental interior. These and other associations, described in §4.2, support the geologic plausibility of the regionalization.

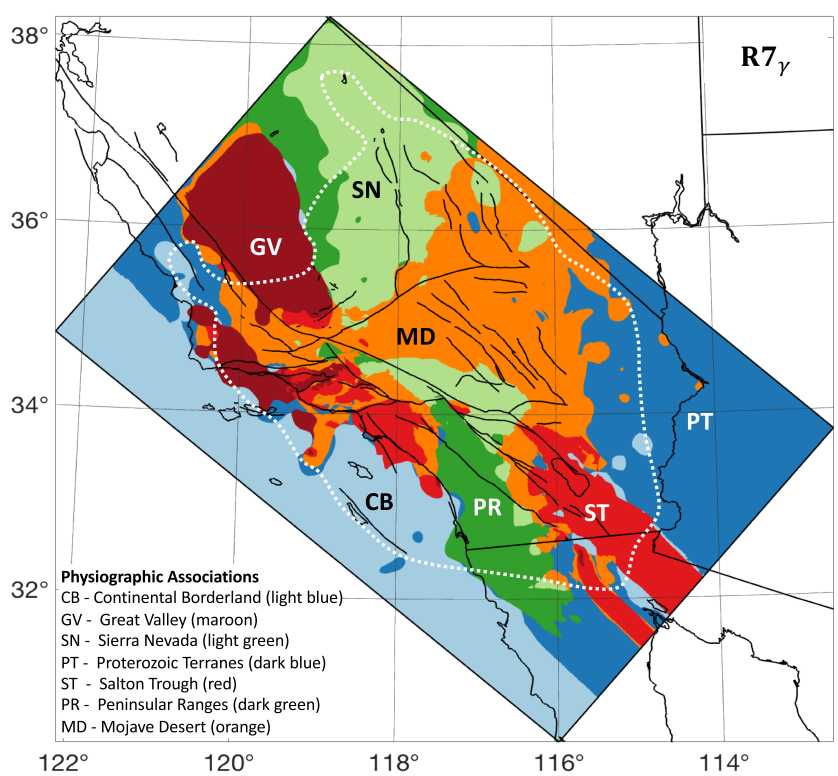

Figure 7. Regionalization version $R7_\gamma$ of the CVM-S4.26 velocity profiles, obtained from the K-means++ clustering algorithm for $K = 7$. The clusters are identified as colored regions on the map and labeled by their associated physiographic provinces. White dotted line encloses the model area where checkerboard tests show the mid-crustal resolution to be relatively good at lateral scale lengths of 15 km.

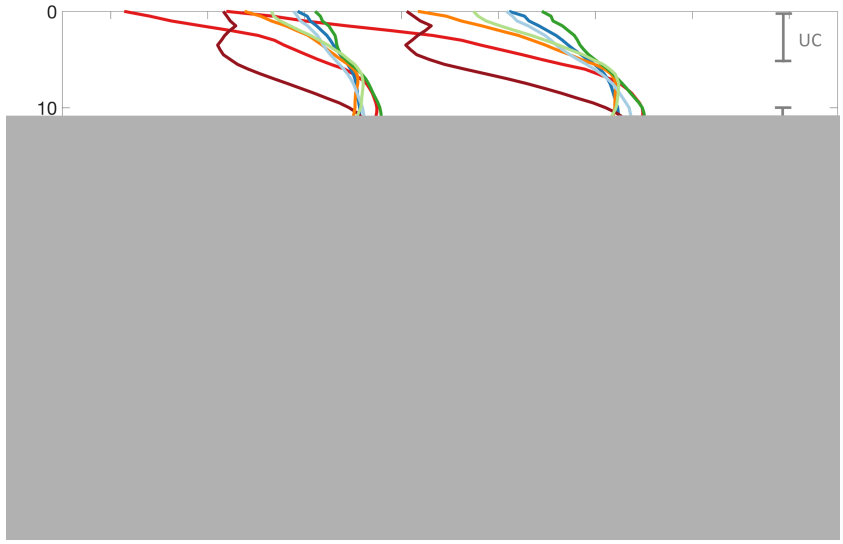

Figure 8. Centroid profiles $\overline{\alpha}^{(k)}(z)$ and $\overline{\beta}^{(k)}(z)$ for the $R7_\gamma$ regionalization. Region colors and two-letter abbreviations are the same as in Figure 7. Gray bars show depth intervals used to compute the upper-crustal (UC), mid-crustal (MC), and lower-crustal (LC) profile averages listed in Table 2.

3.5. Clustering verification and validation

We have explored the robustness of the low-order K-means regionalizations through numerical experiments and comparisons with other observations. Here we describe six robustness properties documented below and in the Supporting Information (S.I.):

1. The clustering results are insensitive to the cluster initialization. Initializations using randomly selected profiles as cluster seeds almost always converged to the same regionalization. As illustrated in Figure S1, experiments using supervised clustering recovered nearly identical regionalizations as unsupervised clustering.
2. The unsupervised regionalizations for $K \leq 7$ from the full CVM-S4.26 study area show good agreement with those obtained from a reduced model domain that excluded the outer one-third of the study area (Figure S2).
3. The agreement between RK_α and RK_β is consistently good for $K \leq 7$ (cf. Figures S3 and S4). The minor differences are largely confined to small-scale features associated with region boundaries or the bubble-like inversion artifacts (Figures S5-S7).
4. The regions defined by the clusters are multiply-connected, but they are largely composed of geographically coherent areas recognizable as distinct physiographic provinces. A given region typically comprises multiple provinces of similar physiography and geology.
5. Region boundaries often conform to major faults, topographic fronts, and geochemical transitions.
6. The progression of regionalizations with K generates a coherent set of structural refinements; each increment of K introduces a new region typically by partitioning a larger region into two smaller regions without reorganizing the other preëxisting regions, or by occupying a transition zone between two regions.

Because the number of regions K is finite and fixed, the objective function must decrease in every step and the K-means algorithm is thus guaranteed to converge to a local minimum. This minimum may not be global, however, owing to the nonlinearity of the classification scheme. Robustness properties (1) and (3) indicate that the global minima are achieved by the CVM-S4.26 regionalizations at the small K values investigated here.

We assessed the robustness of the tomographic clustering to the inherited model bias described in §2.2 by reducing the model domain. Perturbations to tomographic starting models obtained by quadratic optimization tend to be relatively weak and smooth in areas of poor data coverage. If the starting model is also smooth, then the profiles from these areas will be similar, which can bias the cluster centroids. In the case of CVM-S4.26, the poorest tomographic resolution is along the periphery of the model area. We therefore

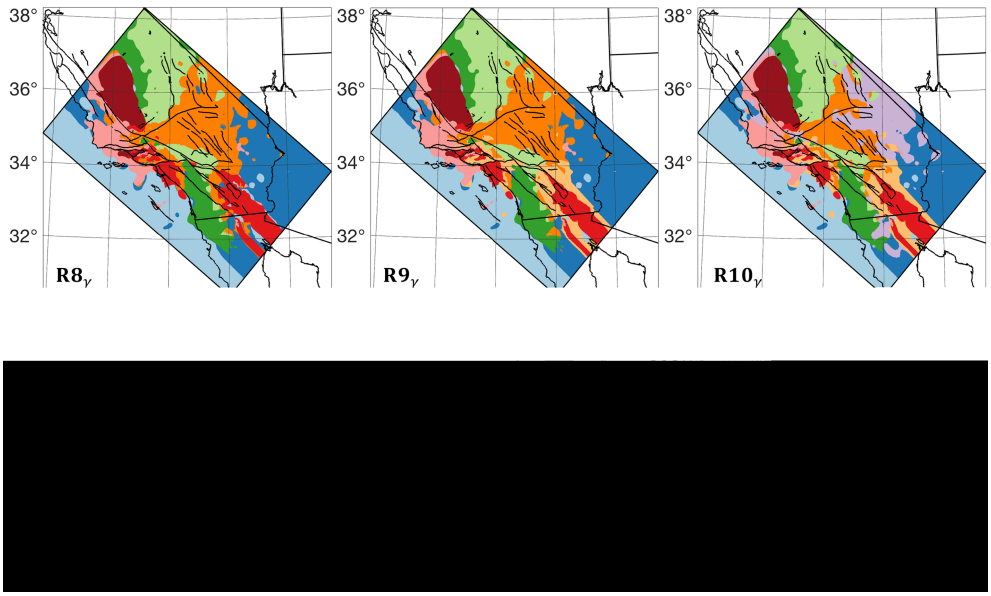

Figure 10. RK_γ regionalizations for $K = 8$-10. The clusters are identified as colored regions on the maps (top panels). The centroid profiles are plotted as functions of depth in corresponding colors (bottom panels).

where necessary and increased the area of deep sedimentary basins ($z_{2.5} > 1$ km) by a factor of about three (Lee & Chen, 2016). Tomographic correlations with structures known from other information are illustrated in Figure 7, where the $R7_\gamma$ regions show strong associations with major physiographic and geologic provinces. The spatial relationships are further investigated in §4.2 and §5.

The coherence of the structural refinements (property 5) supports the robustness of the regional classification. For $K = 3$, the cluster analysis identifies one region (red) comprising the major sedimentary basins; another (light green) extending along the batholithic axis from the Peninsular Ranges across the Mojave Desert and up through the Sierra Nevada; and a remainder (light blue) that includes two large subregions, the off-shore Continental Borderlands and the Proterozoic Terranes of eastern California and western Arizona (Condie, 1982). From the maps in Figure 5 and the S.I., we can see that, with each increment of K from 3 to 7, the cluster analysis for all three profile types, α, β, and γ, reorganizes the regionalizations primarily by partitioning a large region into two smaller regions or by differentiating a transition zone between two regions. In the broad-brush terms, these partitions can be sketched as follows:

- $R4$ differentiates the Continental Borderlands (CB, light blue) from the Proterozoic Terranes (PT, dark blue), extending the latter into the eastern Mojave Desert.
- $R5$ differentiates the Great Valley, Santa Barbara, and Santa Maria basins (GV, purple) from the Salton Trough and Los Angeles basins (ST, red).
- $R6$ differentiates the Mojave Desert and Basin & Range (MD, orange), overprinting a heterogeneous transition zone between the Sierra Nevada (SN, light green) and the Proterozoic Terranes (PT, dark blue) in $R5$.
- $R7$ differentiates the western zones of the Peninsular Ranges and Sierra Nevada batholiths (PR, dark green) from their eastern zones (SN, light green).

The α-β agreement declines for $K > 7$, dropping to 84% at $K = 8$ and to 72% at $K = 9$ (Figure 9). The disagreements are mapped in Figures S3-S5. The areas of α-β disagreement for $R7$ are small and scattered, but those for $R8$ and $R9$ are not. Both $R8_\alpha$ and $R8_\beta$ introduce a new region that includes the Santa Maria Basin and the off-shore Santa Barbara and Ventura basins; however, in the case of $R8_\alpha$, this new region also includes a transition zone between the Mojave and Proterozoic Terranes. In $R9$, the areas of α-β disagreement

Table 2
Regionalized structural properties of $R7_\gamma$.

Region	Mean Elevation (m)	Upper Crust (0-5 km)* α (km/s)	β (km/s)	σ	Middle Crust (10-15 km)* α (km/s)	β (km/s)	σ	Lower Crust (20-25 km)* α (km/s)	β (km/s)	σ	M-Discontinuity Depth (km)
CB	-833	5.45	3.11	0.259	6.42	3.65	0.260	7.55	4.37	0.249	21.0
GV	191	4.16	2.19	0.309	6.43	3.68	0.256	6.86	3.97	0.248	31.5
SN	1716	5.33	3.05	0.257	6.10	3.48	0.258	6.29	3.54	0.267	35.0
PT	468	5.56	3.20	0.252	6.28	3.59	0.258	6.76	3.88	0.255	28.0
PR	743	5.75	3.28	0.257	6.52	3.79	0.245	6.67	3.85	0.250	36.5
ST	94	4.06	2.31	0.261	6.49	3.71	0.257	7.12	4.02	0.266	29.0
MD	789	5.12	2.96	0.249	6.15	3.48	0.265	6.59	3.76	0.259	31.0

*Seismic velocities are averages of the region centroid profiles over the indicated depth ranges.

expand northward into the Basin & Range and southward into the Salton Trough, where $R9_\alpha$ and $R9_\beta$ render rather different regionalizations.

Despite these α-β disagreements, the progression in the partitioning of regions from $R7_\gamma$ to $R10_\gamma$ continues to show physiographic and geologic coherence (Figure 10):

- $R8_\gamma$ differentiates the Santa Maria, Santa Barbara, and offshore Ventura basins (SM, pink) from the GV (purple) and MD (orange) regions, eliminating most of the MD area south of the Great Valley and west of the San Andreas, and confining GV to the Great Valley and the narrow axis of the Ventura Basin.
- $R9_\gamma$ differentiates the Salton Trough and Coachella Valley (ST, red) from the Salton Trough Periphery (SP, yellow). This new region comprises the eastern part of Peninsular Ranges west and south of the physiographic Salton Trough, as well as the Orocopia/Chocolate mountain belt and related terranes northeast of San Andreas Fault.
- $R10_\gamma$ differentiates the Eastern Mojave and Basin & Range (EM, light purple) from the Western Mojave (MD, orange) approximately along the Eastern California Shear Zone.

We will have more to say about these physiographic and geologic correlations in §5.

4. Regionalized structure of Southern California

The application of the K-means++ clustering algorithm to CVM-S4.26 generates a coherent sequence of regionalizations that can be associated with recognized physiographic and geologic provinces of Southern California. The signature of each region is its centroid velocity profile $\overline{\gamma}^{(k)}(z)$. Here we characterize these mean profiles by layer averages and investigate the regional isostatic balance implied by the inferred density profiles.

4.1. Properties of the $R7_\gamma$ velocity profiles

To compare the regionalized velocity profiles, we obtained structural properties of the upper, middle, and lower crust by taking averages of the $R7_\gamma$ centroid profiles $\overline{\boldsymbol{\alpha}}^{(k)}$ and $\overline{\boldsymbol{\beta}}^{(k)}$ over the depth ranges 0-5 km, 10-15 km, and 20-25 km, e.g. denoted $[\alpha_{\mathrm{uc}}^{(k)}, \alpha_{\mathrm{mc}}^{(k)}, \alpha_{\mathrm{lc}}^{(k)}]$, and we computed Poisson's ratio $\sigma = \frac{\alpha^2-2\beta^2}{2(\alpha^2-\beta^2)}$ from these layer averages. We defined the regional depth of the M-discontinuity, $z_{\mathrm{M}}^{(k)}$, as the model depth closest to $\overline{\beta}^{(k)}(z) = 4.3$ km/s, discretized in 0.5 km increments, and we estimated the mean elevation $h^{(k)}$ for each region using the ETOPO1 digital elevation model (Amante & Eakins, 2009). These regionalized properties are listed in Table 2.

The layer values of σ are plotted against the averages of α in Figure 11. Poisson's ratio is highest (0.31) in the sediment-dominated upper crust of the GV region. A similar anomaly is not observed in the ST upper crust, which is also sediment-dominated, suggesting that the GV value may be biased by near-surface structural complexity inherited from the CVM-S4.26 starting model. For all other regions, however, Poisson's ratios are typical of crustal rocks (0.24-0.27) (Brocher, 2005; Christensen, 1996). Among regions for a fixed layer, as well as among layers for a fixed region, the seismic velocities change in approximately equal

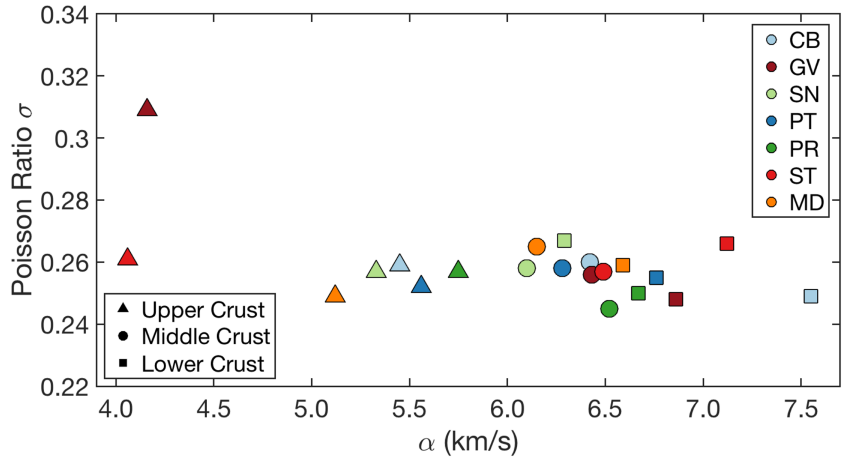

Figure 11. Poisson's ratio σ versus compressional velocity α for the $R7_\gamma$ layer averages of Table 2.

proportions; hence, Poisson's ratio remains fairly constant across the α spectrum. In the two batholithic regions, SN and PR, α goes up by 0.06 km/s and σ by 0.015 from the middle to lower crust, consistent with a decrease in quartz content and an increase in anorthite content (Christensen, 1996). Similarly, the differences between the SN and PR lower crusts, $\Delta\alpha$= 0.38 km/s and $\Delta\sigma$= −0.017, would be explained if the former were more plagioclase-rich and the latter more pyroxene-rich, consistent with the higher velocities and more mafic character of the PR region. These variations in σ are small, however, and their statistical significance is questionable.

The scatter plots of Figure 12 show that the lower-crustal compressional velocities are positively correlated with the mid-crustal compressional velocities and negatively correlated with M-discontinuity depths. The shear velocities display similar relationships, as implied by Figure 11. The first suggests that the loci of the mid-crust and lower crust on the felsic-to-mafic compositional spectrum are positively correlated; i.e., a more mafic lower crust is likely to be overlain by a more mafic mid-crust. The second indicates that the crust is thinner in regions with more mafic lower crust.

4.2. Isostatic model

The property correlations in Figure 12 can be further elucidated by a simple isostatic calculation. For each region k, we estimated the average densities of the three crustal layers $[\rho_{\mathrm{uc}}^{(k)}, \rho_{\mathrm{mc}}^{(k)}, \rho_{\mathrm{lc}}^{(k)}]$ from the velocity depth averages of Table 2 using Brocher's nonlinear ρ-α relationship (2005, equation (1)), and we calculated the

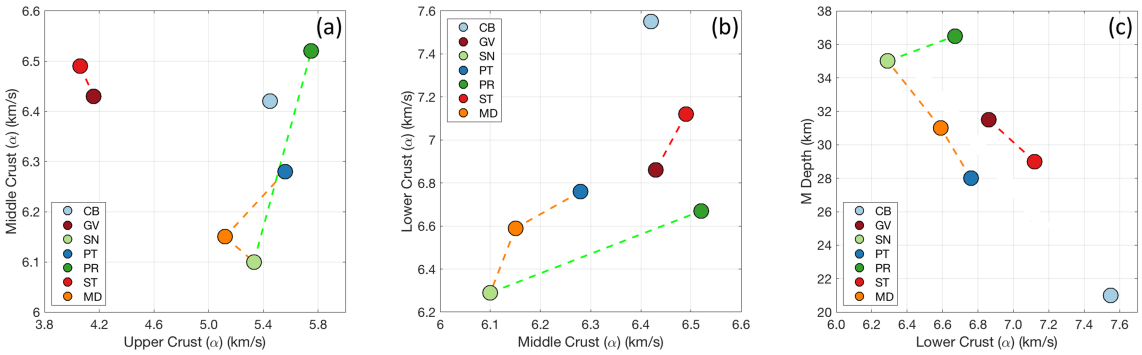

Figure 12. Scatter plots of $R7_\gamma$ region properties from Table 2. Region labels and colors are the same as in Table 1. Colored dashed lines highlight regional comparisons made in the text. **(a)** Middle vs. upper crustal α. The two deeply sedimented regions, GV and ST, show velocities that are low in the upper crust and high in the mid-crust. **(b)** Lower vs. middle crustal α. **(c)** M-discontinuity depth vs. lower crustal α.

area-weighted averages $[\overline{\rho}_{\mathrm{uc}}, \overline{\rho}_{\mathrm{mc}}, \overline{\rho}_{\mathrm{lc}}]$. We assumed that the densities are constant within a layer, in which case the layer mass excesses of the kth region relative to the average are,

$$\Delta M_{\mathrm{uc}}^{(k)} = \left(\rho_{\mathrm{uc}}^{(k)} - \overline{\rho}_{\mathrm{uc}}\right)\Delta z_{\mathrm{uc}} + \left(\rho_{\mathrm{uc}}^{(k)} h^{(k)} - \overline{\rho}_{\mathrm{uc}}\overline{h}\right) - f_{\mathrm{w}}^{(k)}\rho_{\mathrm{w}} h_{\mathrm{w}}^{(k)}, \tag{10}$$

$$\Delta M_{\mathrm{mc}}^{(k)} = \left(\rho_{\mathrm{mc}}^{(k)} - \overline{\rho}_{\mathrm{mc}}\right)\Delta z_{\mathrm{mc}}, \tag{11}$$

$$\Delta M_{\mathrm{lc}}^{(k)} = \left(\rho_{\mathrm{lc}}^{(k)} - \overline{\rho}_{\mathrm{lc}}\right)\Delta z_{\mathrm{lc}} + \left(z_{\mathrm{M}}^{(k)} - \overline{z}_{\mathrm{M}}\right)\left(\overline{\rho}_{\mathrm{um}} - \rho_{\mathrm{lc}}^{(k)}\right). \tag{12}$$

We used the layer thicknesses $\Delta z_{\mathrm{uc}} = 6$ km, $\Delta z_{\mathrm{mc}} = 10$ km, and $\Delta z_{\mathrm{lc}} = 14$ km, the elevations $h^{(k)}$ and M-discontinuity depths $z_{\mathrm{M}}^{(k)}$ given in Table 2, and an average upper mantle density $\overline{\rho}_{\mathrm{um}} = 3,200$ kg/m^3. The last term in equation (10) corrects the upper crustal mass for the fractional area of water $f_{\mathrm{w}}^{(k)}$ of average elevation $h_{\mathrm{w}}^{(k)}$ (a negative number) and density ρ_{w}= 1,000 kg/m^3. We only applied this correction to the CB region, which is largely offshore, where we obtained the region averages $f_{\mathrm{w}}^{(\mathrm{CB})} = 0.90$, $h^{(\mathrm{CB})} = -833$ m, and $h_{\mathrm{w}}^{(\mathrm{CB})} = -890$ m.

We balanced the net crustal mass excess, $\Delta M_{\mathrm{uc}}^{(k)} + \Delta M_{\mathrm{mc}}^{(k)} + \Delta M_{\mathrm{lc}}^{(k)}$, by a mass deficit in the uppermost mantle, taken to be a layer of thickness $\Delta z_{\mathrm{um}} = 30$ km. This lid thickness implies a compensation depth of about 60 km. Writing the upper-mantle mass excess as $\Delta M_{\mathrm{um}}^{(k)} = \left(\rho_{\mathrm{um}}^{(k)} - \overline{\rho}_{\mathrm{um}}\right)\Delta z_{\mathrm{um}} \equiv \Delta\rho_{\mathrm{um}}^{(k)}\Delta z_{\mathrm{um}}$, we can then express isostatic balance as an equation for the regional upper-mantle density anomaly,

$$-\Delta\rho_{\mathrm{um}}^{(k)} = \left[\frac{\Delta M_{\mathrm{uc}}^{(k)} + \Delta M_{\mathrm{mc}}^{(k)}}{\Delta z_{\mathrm{um}}}\right] + \frac{\Delta M_{\mathrm{lc}}^{(k)}}{\Delta z_{\mathrm{um}}}. \tag{13}$$

Figure 13 plots the second term on the right side of equation (13) against the first term (in brackets); the anti-diagonal lines indicate the inferred mantle density anomalies.

The strong anticorrelation of the region values in Figure 13 (Pearson correlation $r = -0.92$) indicates that the lower-crustal mass differences are approximately balanced by those in the upper and middle crust. We see that the regions can be ordered by their projections onto the antidiagonal $\Delta\rho_{\mathrm{um}} = 0$, which range from CB (heavy lower crust) to SN (light lower crust). The fact that this isostatic ordering disperses the regions along the anti-diagonal demonstrates that the diagnostic differences among CVM-S4.26 profiles—i.e., those that govern the relative positions of cluster centroids in $\boldsymbol{\gamma}$-space—are not simply distinctive features confined to the upper crust (e.g., deep sedimentary basin) or the lower crust (e.g., shallow M-discontinuity depth). Instead, tectonic processes, balanced by isostasy, have produced crustal columns with vertically correlated regional properties (e.g., light upper crust implies heavy lower crust). The region-specific correlations of properties across the entire crustal column can be seen directly in the centroid-profile variations of Figure 8. These long-wavelength signatures are easily resolvable by the full-3D tomography, which helps to explain the robustness of the clustering results.

The upper-mantle density anomalies computed assuming isostatic balance vary from −62 kg/m^3 for the CB region to +53 kg/m^3 for the GV region, which lie within the range of upper-mantle density anomalies inferred from Kaban & Mooney's (2001) gravimetric analysis. For example, the positive anomaly we obtain for the SN region (+40 kg/m^3) is roughly consistent with the high upper mantle densities Kaban & Mooney (2001) found for the eastern zone of the Sierra Nevada batholith.

5. Physiographic and geologic correlations

A full interpretation of the regionalization results in the context of California tectonics is beyond the scope of this article (not to mention the competence of its authors). Here we focus on some key features of $R7_{\gamma}$ that can be correlated with previously described geological structures of known tectonic significance. Figure 14 delineates a subset of the regional boundaries, labeled L1 through L13, that we judge to be robust features of the γ regionalizations. The boundary segments remain in approximately the same location when the

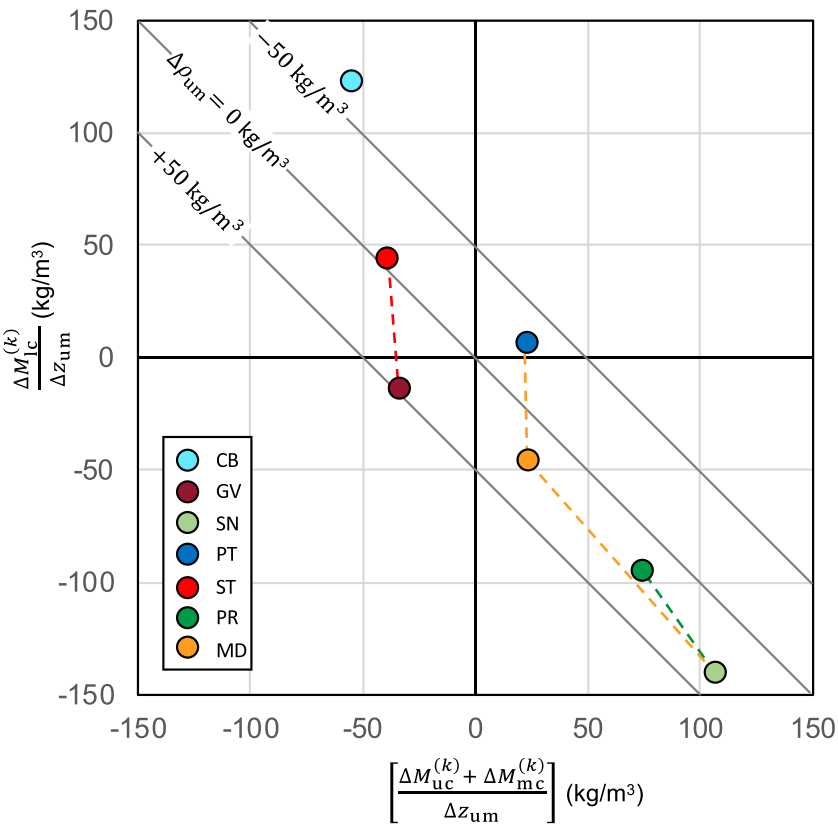

Figure 13. Isostatic balance model for the seven $R7_\gamma$ regions based on the data in Table 2. The abscissa is the combined mass excess of upper and middle crust, and the ordinate is the mass excess of the lower crust, both expressed in upper mantle density units (equation (13)). Diagonal lines plot equal values of the upper-mantle density anomaly ρ_{um}. Colored dashed lines highlight regional comparisons made in the text.

$R7_\gamma$ regionalization is applied to a reduced area that excludes the outer 50 km of the model domain, where the tomographic resolution is poor (Figure S2). Moreover, once a boundary segment appears, it remains a feature of the regionalization as the number of regions increases to at least $K = 10$ (Figure 10). One exception to these generalizations is L5, the MD-PT boundary, where the eastern side of the MD region rotates towards the Eastern California Shear Zone in the trimmed $R7_\gamma$ regionalization and also in $R10_\gamma$. As discussed below, this rotation likely reflects a relatively wide MD-PT gradient zone in the eastern Mojave Desert.

The geographical endpoints of the line segments are listed in Table S2. In this section, we will explore the relationship of the 13 boundary segments in Figure 14 to faults and other structural transitions inferred from geological, geochemical, and geophysical mapping.

5.1. Deep sedimentary basins: GV & ST

Regions GV and ST are characterized by thick sediment columns that form near-surface waveguides with low velocity averages well constrained by the tomography. As noted in §4.1, GV has artificially high surface velocities inherited from the CVM-S4.26 starting model that may contribute to the regional differences. Aside from this near-surface artifact, the upper-crustal average velocities of the two regions are nearly the same (Figure 12a). However, the average mid-crustal and lower-crustal velocities of ST are higher and its M-discontinuity is shallower (Figure 12c).

Similar differences in lower-crustal structure explain the classification of the Santa Maria and Santa Barbara basins as GV and the Los Angeles basins as ST. The near-surface artifact of the GV region is absent in the

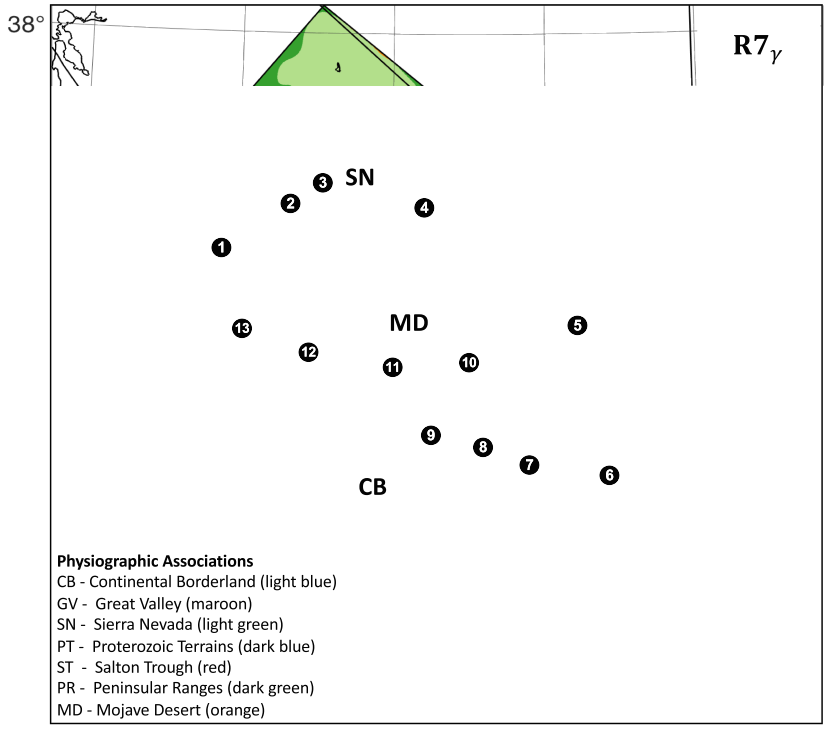

Figure 14. Regionalization map for $R7_\gamma$ annotated with a subset of regional boundaries L1-L13 (dashed white lines) that delineate geologic structures discussed in the text.

Santa Maria Basin (Figure 1e, profile 1). The association of these two provinces in $R7_\gamma$ appears to reflect their geologic similarities; the Santa Maria Basin contains sediments of the Great Valley Group and, like the western Great Valley, is underlain by Franciscan metamorphic rocks (Chapman et al., 2016; Page, 1970). The higher mid-crustal velocities of the Salton Trough and Los Angeles basins are consistent with the emplacement of igneous and metamorphic rocks of more mafic composition during the rifting events that formed these basins (Christensen & Mooney, 1995; Godfrey et al., 2002; Persaud et al., 2016).

At the southwest side of the Great Valley, marked by L1 in Figure 14, the San Andreas Fault separates the Great Valley from the Salinian block. A regional boundary along this line is a consistent feature in all of the *K*-means clustering results (Figures 5, 7, 10; S.I.). L1 separates the GV region from the MD region in $R7_\gamma$. This regionalization largely classifies the Salinian block as MD within the model area where the mid-crustal tomographic resolution is relatively high (Figure 7). Northwest along the axis of the Salinian block, MD transitions to PT and then to CB, but the tomographic coverage in the western part of the model area is poor and more sensitive to areal trimming (Figure S2); for this reason, we discount the tectonic significance of this variable association.

The association of the Salinian Block with the MD region is consistent with the location of the GV-MD boundary marked by L13, which lies on the opposite side of the Salinian block, where the Nacimiento Fault separates granitic rocks from the Santa Maria Basin and its Franciscan basement (Chapman et al., 2016; Page, 1970). The Sur-Nacimiento fault has been variously modeled as a thrust fault (Ducea et al., 2009; Page, 1970), a sinistral strike-slip fault (Jacobson et al., 2011), or low-angle normal (exhumation) fault (Chapman et al., 2016). The association of the Salinian block with a coherent MD region is consistent with the pre-San Andreas palinspastic reconstruction of Chapman et al. (2016) that involves no sinistral motion and places the Nacimiento Franciscan Belt and Santa Maria Basin outboard of the Mojave Desert.

The Ventura Basin is regionalized as a narrow corridor of GV flanked by a larger area of ST. This mixed association, which can also be seen at the southern end of the Great Valley, reflects the close distance between the two centroid profiles (Figure 12). L12 is the ST-MD boundary, which is parallel to the San Cayetano-

Ventura-Pitas Point system of active thrust faults that separates the deep Ventura Basin from Franciscan and Mesozoic granitic basement (Hubbard et al., 2014; Rockwell, 1988). The L12 location is 15-20 km north of the active San Cayetano-Ventura-Pitas Point fault trace, but this is consistent with models in which the thrust ramp flattens into a nearly horizontal décollement at about 7 km depth and then steepens into a high-angle fault (Hubbard et al., 2014; Marshall et al., 2017). The high-angle master fault in the thrust-ramp model collocates with the major crustal boundary at L12. The boundary lies about 30 km south of the Big Pine Mountain Fault, usually identified as the southern limit of the Salinian Block (Chapman et al., 2014; Dickinson, 1996).

L6, which separates ST from PT on the northeast side of the Salton Trough, is another deep-basin boundary persistent across the range of regionalization experiments. This boundary is parallel to the southeastward extrapolation of the present-day San Andreas but offset from it by about 10-15 km to the northeast, consistent with the northeastern dip of the San Andreas Fault in the northern part of the Salton Trough (Fuis et al., 2012, 2017). Near the Mexican border, L6 accurately aligns with the surface trace of the Algodones-Altar fault zone, thought to be the main locus of the North-America-Pacific plate boundary during the Pliocene (Beard et al., 2016; Howard et al., 2015).

Several other fault-controlled edges of deep sedimentary basins correspond to region boundaries. The irregular ST-MD border on the west side of the Salton Trough (L7) roughly aligns with surface exposures of the Western Salton Detachment Fault, a major low-angle normal fault system that Mason et al. (2017) argue was active during the late-Miocene localization of the Pacific-North America plate boundary in the northern Salton Trough. The vertical alignment implied by the regionalization suggests that the low-angle detachment localized along the edge of a major structural boundary.

A major feature of $R7_\gamma$, not marked in Figure 14, is the GV-ST-MD transition that is aligned with the White Wolf Fault at the southern end of the Great Valley. This profound structural transition has a long history of thrust, detachment, and strike-slip faulting (Chapman et al., 2012; Malin et al., 1995).

5.2. The batholithic dichotomy: SN & PR

The composite batholiths of the Sierra Nevada and Peninsular Ranges divide into two juxtaposed belts: an older (ca. 140-100 Ma) western zone of tonalitic/gabbroic plutons that were emplaced into ophiolitic crust and deep-water strata, and a younger (ca. 100–80 Ma) eastern zone of granitic/granodioritic plutons that invaded shallow-water, passive-margin strata (Chapman et al., 2012, 2016; Gromet & Silver, 1987; Jiang & Lee, 2017; Kimbrough et al., 2015; Sharman et al., 2015).

In $R7_\gamma$, this batholithic dichotomy is expressed by the PR-SN cluster division, which occurs for all regionalizations with $K = 7$-10. The SN region comprises the eastern zone of the Sierra Nevada batholith, the central Transverse Ranges, and a narrow, broken-up zone on the eastern side of the Peninsular Range batholith. The PR region comprises the western zones of both batholiths. The integrity of the PR cluster is supported by the potential-field mapping, which shows positive isostatic gravity anomalies and positive geomagnetic anomalies congruent with both of the PR belts. The reader is referred to Figure 3 of Lee, Chen, Jordan, Maechling, et al. k2014), which plots the potential-field data from Simpson et al. (1986) and Roberts and Jachens (1999) on the CVM-S4.26 model grid.

The differences between SN and PR are also reflected in the initial strontium ratios $(^{87}Sr/^{86}Sr)_i$ measured across the batholiths. Geochemists use the initial Sr ratio to distinguish the lithospheric affinities of igneous rocks, usually associating low values ($\lesssim 0.706$) with oceanic lithosphere and high values ($\gtrsim 0.706$) with continental lithosphere (Glazner & O'Neil, 1989; Kistler & Peterman, 1978; Silver et al., 1979). In the central Sierra Nevada, the PR-SN boundary marked by L3 approximates the 0.706 line used by Kistler and Peterman (1978) and Chapman et al. (2012) to separate the western and eastern plutonic zones (Figure 15a). In the Peninsula Ranges, PR-SN boundary marked by L8 lies 20-50 km west of the 0.706 line (Figure 15b), which runs along the San Jacinto Fault (Kistler et al., 2003; Langenheim et al., 2004). However, L8 accurately separates the petrologically distinct western-zone plutons from those of the eastern-zone, as mapped by Jiang and Lee (2017, Figure 1). This eastern PR border also closely tracks the distinct "Peninsular Range Batholith boundary" mapped by Langenheim et al. (2004) using gravimetric and magnetic data. The initial Sr values of rocks west of L8 are generally less than 0.705.

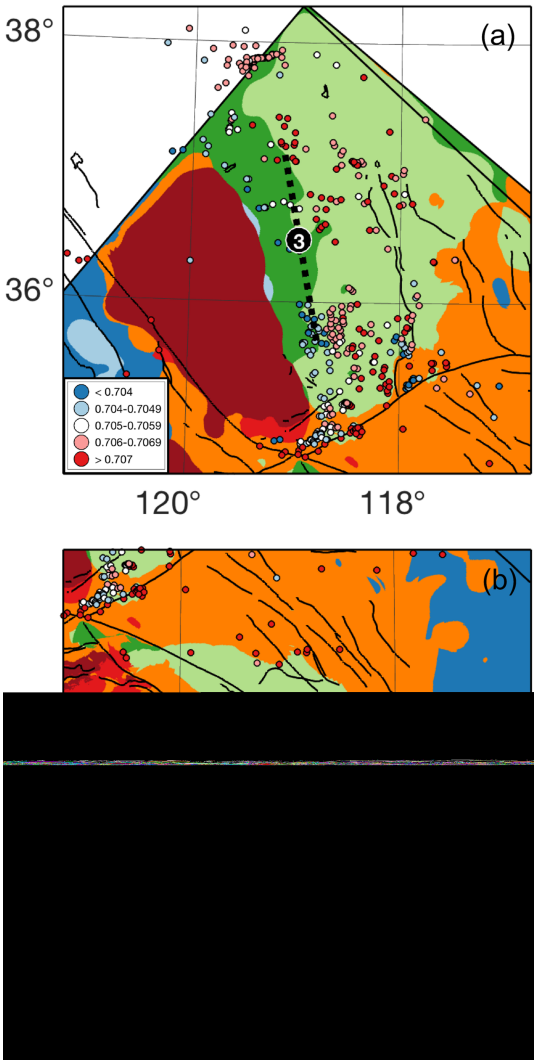

Figure 15. Initial strontium ratios ($^{87}Sr/^{86}Sr)_i$ complied by Chapman (2012) and Kistler et al. (2003), plotted as colored dots on $R7_\gamma$ regionalization maps of (a) the Sierra Nevada batholith and (b) the Peninsular Range batholith. Dashed black lines L3 and L8 mark the boundaries between the SN (light green) and PR (dark green) regions that approximate the division of the two batholiths into eastern and western zones. PR and SN correlate with low and high ($^{87}Sr/^{86}Sr)_i$ values, respectively. Maps are plotted at the same scale.

The centroid PR profile has higher velocities than the centroid SN profile throughout the crust (Table 2, Figure 12). The difference is about 0.4 km/s in the middle and lower crust, which agrees with the more mafic compositions observed in the western plutonic zone. The mantle density anomalies of the two regions obtained from the isostatic model of §4.2 are positive and of similar magnitude, $\Delta\rho_{\mathrm{um}}^{(\mathrm{PR})} = 27\ \mathrm{kg/m^3}$ and $\Delta\rho_{\mathrm{um}}^{(\mathrm{SN})} = 40\ \mathrm{kg/m^3}$, consistent with a denser "arclogite root", or the remnants of such a root, beneath both regions (Saleeby, 2003; Saleeby et al., 2012).

The western border of the batholith at the north end of Peninsular Ranges abuts the sedimentary basins of the Los Angeles area along the PR boundary delineated by L9. The southern part of this line coincides with the Cristianitos Fault (Ehlig, 1979; Klotsko et al., 2015), an element of the San Gabriel-Chino Hills-Cristianitos fault system that acted as the primary transform plate boundary during the late Miocene formation of the Los Angeles Basin (Ingersoll & Rumelhart, 1999). L9 also corresponds to a NNW-striking gravity gradient in Langenheim et al.'s (2006) basement gravity map.

The GV-PR boundary delineated by L2 is a strong feature of the regionalization. It lies buried beneath the Great Valley sediments, where the eastern edge of the deep San Joaquin Basin abuts the western zone of the Sierra Nevada batholith. At these latitudes, the western zone comprises the Paleozoic Kings-Kaweah ophiolite belt, which was accreted to the continent circa 250 Ma and subsequently intruded by Mesozoic plutons (Chapman et al., 2012; Saleeby, 2011). L2 marks a nearly vertical discontinuity between this western plutonic zone and the Great Valley, where forearc strata were deposited above the Middle Jurassic basement of Coast Range ophiolite (Chapman, 2017; Godfrey & Klemperer, 1998). The mantle component of this ophiolite has been juxtaposed against the western zone at mid-crustal depths, forming a high-velocity anomaly that dips gently westward and widens beneath the Great Valley (Figure 1b).

5.3. Central Transverse Ranges: SN

A large area comprising the San Gorgonio Massif, the San Bernardino Mountains, and the eastern San Gabriel Mountains persistently associates with SN in all of the regionalization experiments (e.g., light green near the center of Figures 7 & 13). The central Transverse Ranges are known to have high crustal thicknesses and low crustal velocities, comparable to those of the Sierra Nevada batholith (Figure 4; Zhu & Kanamori, 2000; Yan & Clayton, 2007). Like the Sierra Nevada, they have negative isostatic gravity anomalies, indicating crustal compositional buoyancy.

On the south side of the central Transverse Ranges, the SN region includes the topographically elevated San Gorgonio, Yucaipa Ridge-Wilson Creek, and Morongo blocks that are moving relative to one another along the Mill Creek and Mission Creek strands of the San Andreas fault system (Spotila et al., 1998). This "San Gorgonio knot" forms the largest restraining step in the San Andreas Fault (Yule, 2009) and questions remain about the mechanical role it might play in governing the length of ruptures on the southern San Andreas (Beyer et al., 2018; Heermance & Yule, 2017). The SN region comprises the Big Bear block north of the San Andreas, blocks within the knot, and also the eastern zone of the Peninsular Ranges south of the San Andreas and east of L8 (Figure 14). This association is consistent with the potential-field modeling of Langenheim et al. (2005), who inferred that eastern-zone Peninsular Ranges basement rocks have been wedged above the basement of the central Transverse Ranges in a layered structure that extends at least 10 km south of the Banning fault segment of the San Andreas.

The knot thus appears to be a complication in the San Andreas kinematics as it jumps from inboard to outboard of the eastern batholithic zone, perhaps related to the rheology of this region's thicker, more felsic lower crust (Lyakhovsky & Ben-Zion, 2009). This kinematic resistance of the Central Transverse Ranges to translation by the San Andreas Fault likely plays a role in the partitioning of San Andreas motion onto the San Jacinto Fault and the Eastern California Shear Zone (Ozakin & Ben-Zion, 2015).

The SN-MD boundary on the north side of the Central Transverse Ranges (marked as L10 in Figure 14) coincides with the North Frontal Thrust of the San Bernardino Mountains (Meisling & Weldon, 1989; Spotila & Sieh, 2000). The frontal thrust system turns south near 117.2°W, forming the west side of the Big Bear Plateau, whereas the SN region extends westward across the lower topography of the southern Mojave block. Its northern boundary with MD meets the San Andreas Fault near Palmdale. This westward extension is consistent with seismic data showing a thick, low-velocity crust north of the San Gabriel Mountains on the Mojave side of the San Andreas Fault (Zhu, 2000). Combining the LARSE-I refraction lines with receiver functions stacked at SCSN stations, Yan and Clayton (2007) concluded that "the deep root of the San Bernardino Mountains most probably extends farther to the NW, where no surficial topography high exists," consistent with the regionalization results. The topographic difference remains unexplained, however.

The SN region of the central Transverse Ranges includes the eastern San Gabriel Mountains. Given the small area of overlap, this could be spurious association. It is interesting to note, however, that the western SN boundary, delineated by L11, aligns with a NW-trending reflector that Fuis Ryberg, Lutter, and Ehlig (2001) observed in the LARSE-I data and associated with the Vincent Fault. The Vincent Fault, once identified as a possible remnant of the Laramide subduction megathrust, has been recently reinterpreted as a shallow-angle normal fault involved in the exhumation of the Pelona Schist (Xia & Platt, 2018). Schists of this type are thought to underlie the San Gabriel Mountains at mid-crustal depths, where they have been associated with bright reflectors characterized by velocity inversions (Ryberg & Fuis, 1998). These reflectors could be the top of or within an MC-LVZ containing low-velocity Pelona Schist (Fuis, Ryberg, Godfrey, et al., 2001). The MC-LVZ of CVM-S4.26 is well expressed in the San Gabriel Mountains west of the Vincent Fault but weak in the SN crust of the central Transverse Ranges (Figure 3), consistent with Fuis, Ryberg, Godfrey, et al.'s (2001) conclusion that the Pelona Schist is not present at depth along the LARSE-I transect in the Mojave Desert.

5.4. The Continental Lithospheric Domain: SN, MD, and PT

The three $R7_\gamma$ regions SN, MD, and PT include almost all of the upper crust in the study region known to be composed of igneous and metamorphic rocks derived from continental lithosphere; taken together, they form the "continental lithospheric domain" of Southern California. To a first approximation, the boundary of the SN-MD-PT super-region is congruent with the Sr 0.706 line (Figure 15; see also Chapman et al., 2014, Figure 1). The crustal properties among the three regions of this domain (connected by orange dashed lines in Figures 12 & 13) show a variation SN→MD→PT from a thicker, more felsic crust to a thinner, more mafic crust.

The upper-crustal velocities of the three regions are similar and consistent with cracked rocks of felsic composition at low-pressure (Brocher, 2005; McCaffree Pellerin & Christensen, 1998); the upper-crustal densities inferred from Brocher's (2005) relation differ by only a few percent. The lower-crustal α increases from 6.3 km/s for SN to 6.6 km/s for MD to 6.8 km/s for PT, spanning a range from felsic granulite to mafic granulite in Christensen and Mooney's (1995) compositional spectrum. The mid-crust shows the same regional progression, although the velocity differences are only about one-third as large (Figure 12b). The M-discontinuity depths, which decrease from 35 km for SN to 28 km for PT, are inversely correlated with the lower crustal velocity (Figure 12c). According to the isostatic model of Figure 13, the mantle density of PT is lower than that of SN and MD by about 60 kg/m^3, consistent with either eclogitic depletion of the uppermost mantle beneath PT or eclogitic enrichment beneath SN and MD, or both.

The crustal variation in the sequence SN→MD→PT can be explained by progressive crustal thinning accompanied by basaltic intrusion and densification of the lower and middle crust (e.g., Lachenbruch et al., 1994). According to this hypothesis, all three regions started with a thick, buoyant continental crust developed in the Mesozoic along convergent margin of the California Arc (Ducea et al., 2009; Tosdal & Wooden, 2015); subsequent extension thinned and densified PT more than MD, and MD more than SN. This ordering is

consistent with the observed increase in heat flow from SN to MD to PT (Bonner et al., 2003; Sass et al., 1994). The primary mechanism that drove the regional extension is thought to be the gravitational collapse of orogenically over-thickened crust (Chapman et al., 2012; Rey et al., 2001; Saleeby, 2003). Within each region, extension was accommodated by detachment normal faulting in the upper crust and ductile flow in the lower crust (Brun et al., 2018; Davis & Lister, 1988; Platt et al., 2015; Wernicke & Axen, 1988).

This hierarchical regional structure is reflected in the regional boundaries internal to the continental domain. The boundaries separating SN from MD along lines L4 and L10 are both expressed as topographic fronts, where the more buoyant SN region stands higher than MD (Table 2). As we have noted, L10 coincides with the North Frontal Thrust of the San Bernardino Mountains.

L4 is an interesting lineament. It aligns with an irregular topographic front, expressed by the topographic gradient at 1,300 m contour, which cuts SSW-NNE across the Death Valley/Panamint Valley extensional domain at a high angle to the SSE-NNW axis of the late-Cenozoic pull-apart basins (Andrew & Walker, 2009; Norton, 2011). The L4 boundary corresponds to a strong Bouguer gravity gradient that marks the transition from the thicker SN crust to the thinner MD crust (Kucks, 1999). Its geologic expression is more cryptic, but it may be associated with a northeast-trending segment of the Early Permian continental margin, where compression was accommodated by faults of the southeast-verging Last Chance thrust system (Stevens & Stone, 2005).

The boundary between MD and PT in the eastern Mojave Desert, marked by L5, runs approximately north-south along a longitude of 115.6°. This transition is probably not a sharp boundary, as indicated by the bubble-like appearances of MD in the PT region; moreover, the model-trimming experiment of Figure S2 suggests that its location may be biased eastward by the inherited structure of the PT region. Evidence for a lithospheric boundary in the eastern Mojave has been documented by Miller et al. (2000), who found that the geochemical signatures of Miocene basalts east of about 116°W indicate an ancient (Proterozoic) enriched lithospheric source, whereas the signature of enriched-mantle lithosphere appears to be absent west of this longitude. They also note that the dominant orientation of mountain ranges changes at this longitude and that it marks the eastern limit of schist exposures.

5.5. The Schist Problem

The Pelona-Orocopia-Rand schists of Late Cretaceous/Early Cenozoic age outcrop along detachment structures beneath older crystalline rocks at a number of localities east and west of the San Andreas Fault (Ehlig, 1968; Haxel & Dillon, 1978; Chapman et al., 2016). Geologists have hypothesized that the once-continuous California Arc was disrupted by Laramide subduction of an oceanic plateau in a 500-km-wide corridor between the southern Sierra Nevada and northern Peninsular Ranges (Saleeby, 2003; Saleeby et al., 2007; Nadin & Saleeby, 2008; Chapman et al., 2012). Comparing $R7_\gamma$ with Chapman's (2017) pre-San Andreas palinspastic reconstruction shows that this batholithic gap is filled primarily by crust associated with the MD region.

According to this tectonic hypothesis, flat-slab subduction erosion removed the westernmost arc and inner forearc basin, as well as the sub-batholithic mantle lithosphere, shutting down arc magmatism and thickening the overriding crust. Detritus shed into the trench from the elevated, thickened crust formed the schist protoliths, which were then underthrust beneath the extinguished arc and accreted to its lower crust. Extension associated with the gravitational collapse of the elevated crust in the Late Cretaceous initiated large-scale detachment faulting that exhumed the schists to mid-crustal levels by the early Tertiary (Chapman, 2017; Chapman et al., 2012; Jacobson et al., 2011). Miller et al. (2000) speculate that 116°W marks a decrease in the overall strength of the lithosphere owing to the presence of mechanically weak Pelona-Orocopia-Rand schists in the crustal column to the west of this longitude. The hypothesis thus predicts that the upper-crustal igneous rocks of the MD region are underlain by schists at mid-crustal depths.

McCaffree Pellerin and Christensen (1998) describe three seismological signatures of the schists: low average velocities ($\alpha \approx 5.83$ km/s, $\beta \approx 3.48$ km/s), low Poisson's ratio ($\sigma \approx 0.22$), and high shear-wave anisotropy (5-20%). Some studies of the Mojave block using seismic reflections (Cheadle et al., 1986; Malin et al., 1995), seismic anisotropy (Porter et al., 2011), and seismicity (Magistrale & Zhou, 1996) have supported the schist model, whereas others, such as Hauksson's (2000) tomography, provide little evidence for a widespread distribution of schist. The schist has been identified with bright reflectors imaged locally along the LARSE-I

line in the San Gabriel Mountains, though such reflectors appear to be absent along this line north of the San Andreas Fault (Fuis, Ryberg, Godfrey, et al., 2001).

As Lee, Chen, Jordan, Maechling, et al. (2014) pointed out, the presence of the schist is likely to be associated with the MC-LVZ of CVM-S4.26. The MD region shows a shallow low-velocity channel (Figure 8), but its mid-crustal compressional velocity (6.15 km/s) and Poisson's ratio (0.26) are more consistent with a granitic gneiss than a schist (Christensen & Mooney, 1995; McCaffree Pellerin & Christensen, 1998). On the regional scale, the average schist fraction of MD mid-crust is likely to be rather small. Locally, however, velocities within the channel drop to values consistent with a much larger fraction of schist. The MC-LVZ is particularly well expressed in the southern Sierra Nevada, the western Mojave block, and beneath the Los Angeles and San Gabriel basins (Figure 3). This central part of the study area is where a schist-rich mid-crust is most likely to be found.

6. Conclusions

Our goal has been to map the variations in the crustal structure of Southern California on horizontal scales larger than the crustal thickness but smaller than the width of the North America-Pacific plate-boundary deformation zone. In this exploratory study, we applied *K*-means cluster analysis to a single tomographic model, CVM-S4.26. We did not attempt to characterize the aleatory variability of the tomographic imaging (e.g., due to seismic noise) or its epistemic uncertainty (e.g., due to modeling limitations), nor did we fully assess the effects of the model uncertainties on the cluster partitioning. Cluster analysis is a machine-learning technique susceptible to various types of bias, such as the inheritance bias due to poor data coverage on the periphery of the study area. Although we have tested the robustness of the regionalizations to this particular type of bias, our understanding of the clustering uncertainties is as yet rudimentary, and some of the associations we have drawn from CVM-S4.26 may turn out to be spurious.

An obvious next step towards validating the regional distinctions mapped here will be to compare the CVM-S4.26 clusters with those derived in a similar way from other tomographic models of Southern California, such as CVM-H15.1 (Shaw et al., 2015). These two SCEC-curated velocity models display substantial differences in crustal structure. For example, CVM-H15.1 is based on the Tape et al. (2012) M-discontinuity surface shown in Figure 4a, whereas CVM-S4.26 produces the surface in Figure 4b. Comparing regionalizations from alternative crustal velocity models should help to assess how epistemic uncertainties in the underlying 3D structure translate into uncertainties in 2D regionalizations.

Despite the limitations of this exploratory study, we are encouraged by its results. The *K*-means cluster analysis produces regionalizations that generally conform to the large-scale physiographic provinces of Southern California, and it does a good job in recognizing major tectonic features previously identified by geological, geochemical, and potential-field mapping, active-source profiling, and tomographic imaging. Notable examples from our seven-region model $R7_\gamma$ include faults bounding the deep sedimentary basins of the GV and ST regions, as well as the west-east compositional dichotomy of the California batholith, represented by PR (western zone) and SN (eastern zone).

The three regions SN, MD, and PT comprise almost all of the upper-crustal igneous and metamorphic rocks in the CVM-S4.26 study area that show geochemical signatures derived from continental lithosphere. Our geophysical regionalization is thus consistent with the continent-ocean dichotomy expressed in the hard-rock geochemistry of Southern California. Lower-crustal seismic velocities within this continental lithospheric domain are negatively correlated with crustal thicknesses, yet the crustal columns of the three regions are in approximate isostatic balance. These properties are consistent with an interpretation of SN→MD→PT as a regional progression in the extensional thinning of the crust and the concomitant mafic densification of the lower crust.

All of the $R7_\gamma$ regions except CB comprise multiple provinces with similar physiographic and geologic characteristics (Table 1). In some cases, the provinces have a common tectogenesis; e.g., the east-west (SN-PR) dichotomy of the Sierra Nevada and Peninsular Range batholiths, and the association of Santa Maria Basin with the Great Valley in the GV region. In other cases, the similarity of the tectonic pathways is less obvious; e.g., the association of the Los Angeles basins with the Salton Trough as distinct components of the ST region.

This raises a general caveat. Only the present-day structure of the crust can be directly observed; hence, any tomographic regionalization can only be interpreted as the net product of long-term tectonic activity. Subregions are not required to share a common tectonic evolution, only similar velocity profiles. Each region may, in principle, contain multiple provinces that evolved along different tectonic pathways. That said, inter-region associations among geologic provinces, such as those seen in Figure 7, should stimulate further scrutiny of the tectonic commonalities that might explain these associations.

One commonality is regional isostasy. From the centroid velocity profiles and mean elevations, we constructed an isostatic model and found that the regionalized crustal columns are in approximate isostatic balance (Figure 13). The mass anomalies of the upper and middle crust correlate negatively with lower-crustal mass anomalies, and the mantle density anomalies required for exact balance are within the range inferred from petrologic data for eclogitic enrichment and depletion of the mantle lid. The dispersion of regions along the anti-diagonal of Figure 13 demonstrates that the diagnostic differences among CVM-S4.26 profiles are not simply distinctive features confined to the upper crust or the lower crust, but rather region-wide properties vertically correlated across the entire crustal column. These regional signatures are characterized by correlated variations of seismic velocities in crustal layers with dimensions comparable to the crustal thickness —a vertical scale that is easily resolved by the CVM-S4.26 inversions in areas of good wavepath coverage (Lee, Chen, Jordan, Maechling, et al., 2014). The ability of the full-3D tomography to distinguish these nearly isostatic crustal signatures helps to explain the robustness of the regionalization results.

Well-constrained regional boundaries obtained from a whole-crust profile analysis match major faults, topographic fronts, and geochemical transitions mapped at or near the surface. These results indicate that major lateral transitions in the crustal structure of Southern California are fairly narrow features that are nearly vertically aligned throughout the crust. In some cases, the vertical alignment is to be expected, such as along the strike-slip fault boundaries of the deep sedimentary basins (e.g., L1 and L6). The near verticality of other boundaries is perhaps more surprising, such as the SN-MD boundaries marked by L4 and L10. As we have shown, potential-field modeling supports the geographic localization of these transitions.

Therefore, in Southern California, the remarkable alignment of regional boundaries with mapped surficial features suggests that the horizontal scale of the regional transitions is typically on the order of, or less than, a crustal thickness. We conclude that the crustal boundaries delineated in Figure 14 are high-angle structures marking relatively narrow transition zones between the characteristic crustal columns of the juxtaposed regions. One exception to this generalization is the MD-PT transition marked by L5, which may extend over a zone in the eastern Mojave several times wider than the crustal thickness.

Acknowledgments
We thank David Okaya, Francis Wu, Katie Ardill, and John Platt for helpful discussions and Carl Tape and an anonymous reviewer for helpful reviews. The CVM-S4.26 model can be accessed at https://github.com/SCECcode/ucvmc. The main analysis tool is the *K*-means++ algorithm implemented in MATLAB® and documented at https://www.mathworks.com/help/stats/kmeans.html. Output files of the regionalizations can be downloaded at https://github.com/eymold/S426_Kmeans/releases (v.1.0.0 DOI: 10.5281/zenodo.3525443. This research was supported by the Southern California Earthquake Center (SCEC) under National Science Foundation Cooperative Agreement EAR-1600087, US Geological Survey Cooperative Agreement G17AC00047, and grants from the W. M. Keck Foundation and Pacific Gas & Electric Company. The SCEC contribution number for this paper is 9008.

References

Allam, A. A., & Ben-Zion, Y. (2012). Seismic velocity structures in the southern California plate-boundary environment from double-difference tomography. *Geophysical Journal International*, *190*(2), 1181–1196. https://doi.org/10.1111/j.1365-246X.2012.05544.x

Amante, C., & Eakins, B. W. (2009). *ETOPO1 1 Arc-Minute Global Relief Model: Procedures, Data Sources and Analysis*, NOAA Technical Memorandum NESDIS NGDC-24. Washington DC: National Oceanic and Atmospheric Administration.

Andrew, J. E., & Walker, J. D. (2009). Reconstructing late Cenozoic deformation in central Panamint Valley, California: Evolution of slip partitioning in the Walker Lane. *Geosphere*, *5*(3), 172–198. https://doi.org/10.1130/GES00178.1

Arthur, D., & Vassilvitskii, S. (2007). K-means++: The advantages of careful seeding. In *Proceedings of the eighteenth annual ACM-SIAM symposium on Discrete algorithms* (pp. 1027–1035). Society for Industrial and Applied Mathematics.

Atwater, T. (1970). Implications of plate tectonics for the Cenozoic tectonic evolution of western North America. *Geological Society of America Bulletin*, *81*(12), 3513–3536. https://doi.org/10.1130/0016-7606(1970)81[3513:IOPTFT]2.0.CO;2

Beard, S., Haxel, G. B., Dorsey, R. J., McDougall, K. A., & Jacobsen, C. E. (2016). Late Neogene deformation of the Chocolate Mountains Anticlinorium: Implications for deposition of the Bouse Formation and early evolution of the Lower Colorado River. In *30th Annual Desert Symposium* (pp. 176–184). http://pubs.er.usgs.gov/publication/70169150

Beyer, J., Cooke, M. L., & Marshall, S. T. (2018). Sensitivity of deformation to activity along the Mill Creek and Mission Creek strands of the southern San Andreas fault. *Geosphere*, *14*(6), 2296–2310. https://doi.org/10.1130/GES01666.1

Bonner, J. L., Blackwell, D. D., & Herrin, E. T. (2003). Thermal constraints on earthquake depths in California. *Bulletin of the Seismological Society of America*, *93*(6), 2333–2354. https://doi.org/10.1785/0120030041

Brocher, T. M. (2005). Empirical relations between elastic wavespeeds and density in the Earth's crust. *Bulletin of the Seismological Society of America*, *95*(6), 2081–2092. https://doi.org/10.1785/0120050077

Brun, J.-P., Sokoutis, D., Tirel, C., Gueydan, F., Van Den Driessche, J., & Beslier, M.-O. (2018). Crustal versus mantle core complexes. *Tectonophysics*, *746*, 22–45. https://doi.org/10.1016/j.tecto.2017.09.017

California Geological Survey (2010). Geological map of California, https://maps.conservation.ca.gov/cgs/gmc/

Campbell, K. W., & Bozorgnia, Y. (2008). NGA ground motion model for the geometric mean horizontal component of PGA, PGV, PGD and 5% damped linear elastic response spectra for periods ranging from 0.01 to 10 s. *Earthquake Spectra*, *24*(1), 139–171. https://doi.org/10.1193/1.2857546

Campbell, K. W., & Bozorgnia, Y. (2014). NGA-West2 ground motion model for the average horizontal components of PGA, PGV, and 5%-damped linear acceleration response spectra. *Earthquake Spectra*, *30*(3), 1087–1115. https://doi.org/10.1193/062913EQS175M

Chapman, A. D. (2012). *Late Cretaceous Gravitational Collapse of the Southern Sierra Nevada Batholith and Adjacent Areas Above Underplated Schists*. Pasadena, CA: Southern California. Ph.D. Dissertation, California Institute of Technology. http://resolver.caltech.edu/CaltechTHESIS:07212011-115223871

Chapman, A. D. (2017). The Pelona–Orocopia–Rand and related schists of southern California: a review of the best-known archive of shallow subduction on the planet. *International Geology Review*, *59*(5-6), 664–701. https://doi.org/10.1080/00206814.2016.1230836

Chapman, A. D., Ducea, M. N., Kidder, S., & Petrescu, L. (2014). Geochemical constraints on the petrogenesis of the Salinian arc, central California: Implications for the origin of intermediate magmas. *Lithos*, *200-201*, 126–141. https://doi.org/10.1016/j.lithos.2014.04.011

Chapman, A. D., Jacobson, C. E., Ernst, W. G., Grove, M., Dumitru, T., Hourigan, J., & Ducea, M. N. (2016). Assembling the world's type shallow subduction complex: Detrital zircon geochronologic constraints on the origin of the Nacimiento block, central California Coast Ranges. *Geosphere*, *12*(2), 533–557. https://doi.org/10.1130/GES01257.1

Chapman, A. D., Saleeby, J. B., Wood, D. J., Piasecki, A., Kidder, S., Ducea, M. N., & Farley, K. A. (2012). Late Cretaceous gravitational collapse of the southern Sierra Nevada batholith, California. *Geosphere*, *8*(2), 314–341. https://doi.org/10.1130/GES00740.1

Cheadle, M. J., Czuchra, B. L., Byrne, T., Ando, C. J., Oliver, J. E., Brown, L. D., et al. (1986). The deep crustal structure of the Mojave Desert, California, from COCORP seismic reflection data. *Tectonics*, *5*(2), 293–320. https://doi.org/10.1029/TC005i002p00293

Chen, P., Zhao, L., & Jordan, T. H. (2007). Full 3D tomography for the crustal structure of the Los Angeles region. *Bulletin of the Seismological Society of America*, *97*(4), 1094–1120. https://doi.org/10.1785/0120060222

Chen, Y.-S., Weatherill, G., Pagani, M., & Cotton, F. (2018). A transparent and data-driven global tectonic regionalization model for seismic hazard assessment. *Geophysical Journal International*, *213*(2), 1263–1280. https://doi.org/10.1093/gji/ggy005

Christensen, N. I. (1996). Poisson's ratio and crustal seismology. *Journal of Geophysical Research - Solid Earth*, *101*(B2), 3139–3156. https://doi.org/10.1029/95JB03446

Christensen, N. I., & Mooney, W. D. (1995). Seismic velocity structure and composition of the continental crust: A global view. *Journal of Geophysical Research - Solid Earth*, *100*(B6), 9761–9788. https://doi.org/10.1029/95JB00259

Condie, K. C. (1982). Plate-tectonics model for Proterozoic continental accretion in the southwestern United States. *Geology*, *10*(1), 37–42. https://doi.org/10.1130/0091-7613(1982)10<37:PMFPCA>2.0.CO;2

Davis, G. A., & Lister, G. S. (1988). Detachment faulting in continental extension; perspectives from the southwestern U.S. Cordillera. In S. P. Clark, Jr., B. C. Burchfiel, & J. Suppe (Eds.), *Processes in Continental Lithospheric Deformation*, *Geological Society of America Special Paper* (Vol. 218, pp. 133–159). Boulder, Colorado: Geological Society of America. https://doi.org/10.1130/SPE218-p133

Dickinson, W. R. (1996). *Kinematics of transrotational tectonism in the California Transverse Ranges and its contribution to cumulative slip along the San Andreas transform fault system*, *Geological Society of America Special Paper 305* (p. 46). Boulder, Colorado: Geological Society of America.

Ducea, M. N., Kidder, S., Chesley, J. T., & Saleeby, J. B. (2009). Tectonic underplating of trench sediments beneath magmatic arcs: The central California example. *International Geology Review*, *51*(1), 1–26. https://doi.org/10.1080/00206810802602767

Ehlig, P. (1979). The Late Cenozoic evolution of the Capistrano Embayment. In D. L. Fife (Ed.), *Geology Guide to San Onofre Nuclear Station and Adjacent Regions of Southern California*, *Pacific Sections* (pp. 38–46). American Association of Petroleum Geologists, SEPM, and Society of Exploration Geophysicists.

Ehlig, P. L. (1968). Causes of distribution of Pelona, Rand, and Orocopia schist along the San Andreas and Garlock faults. In W. R. Dickinson, & A. Grantz (Eds.), *Proceedings of the Conference on Geological Problems of the San Andreas Fault System* (Vol. 11, pp. 294–305). Stanford, CA: Stanford University Publications in the Geological Sciences

Fliedner, M. M., Klemperer, S. L., & Christensen, N. I. (2000). Three-dimensional seismic model of the Sierra Nevada arc, California, and its implications for crustal and upper mantle composition. *Journal of Geophysical Research - Solid Earth*, *105*(B5), 10,899–10,921. https://doi.org/10.1029/2000JB900029

Fuis, G. S., Bauer, K., Goldman, M. R., Ryberg, T., Langenheim, V. E., Scheirer, D. S., et al. (2017). Subsurface geometry of the San Andreas Fault in Southern California: Results from the Salton Seismic Imaging Project (SSIP) and strong ground motion expectations. *Bulletin of the Seismological Society of America*, *107*, 1642–1662. http://doi.org/10.1785/0120160309

Fuis, G. S., Ryberg, T., Godfrey, N. J., Okaya, D. A., & Murphy, J. M. (2001). Crustal structure and tectonics from the Los Angeles Basin to the Mojave Desert, Southern California. *Geology*, *29*(1), 15–18. https://doi.org/10.1130/0091-7613(2001)029<0015:CSATFT>2.0.CO;2

Fuis, G. S., Ryberg, T., Lutter, W. J., & Ehlig, P. L. (2001). Seismic mapping of shallow fault zones in the San Gabriel Mountains from the Los Angeles Region Seismic Experiment, southern California. *Journal of Geophysical Research - Solid Earth*, *106*(B4), 6549–6568. https://doi.org/10.1029/2000JB900189

Fuis, G. S., Scheirer, D. S., Langenheim, V. E., & Kohler, M. D. (2012). A new perspective on the geometry of the San Andreas Fault in Southern California and Its relationship to lithospheric structure. *Bulletin of the Seismological Society of America*, *102*(1), 236–251. https://doi.org/10.1785/0120110041

Glazner, A. F., & O'Neil, J. R. (1989). Crustal structure of the Mojave Desert, California: Inferences from Sr and O isotope studies of Miocene volcanic rocks. *Journal of Geophysical Research*, *94*(B6), 7861–7870. https://doi.org/10.1029/JB094iB06p07861

Godfrey, N. J., Beaudoin, C., & Klemperer, S. L. (1997). Ophiolitic basement to the Great Valley forearc basin, California, from seismic and gravity data: Implications for crustal growth at the North American continental margin. *Geological Society of America Bulletin*, *109*(12), 1536–1562. https://doi.org/10.1130/0016-7606(1997)109<1536:OBTTGV>2.3.CO;2

Godfrey, N. J., Fuis, G. S., Langenheim, V., Okaya, D. A., & Brocher, T. M. (2002). Lower crustal deformation beneath the central Transverse Ranges, southern California: Results from the Los Angeles Region Seismic Experiment. *Journal of Geophysical Research - Solid Earth*, *107*(B7), ETG 8-1–ETG 8-19. https://doi.org/10.1029/2001JB000354

Godfrey, N. J., & Klemperer, S. L. (1998). Ophiolitic basement to a forearc basin and implications for continental growth: The Coast Range/Great Valley ophiolite, California. *Tectonics*, *17*(4), 558–570. https://doi.org/10.1029/98TC01536

Gromet, P., & Silver, L. T. (1987). REE variations across the Peninsular Ranges batholith: Implications for batholithic petrogenesis and crustal growth in magmatic arcs. *Journal of Petrology*, *28*(1), 75–125. https://doi.org/10.1093/petrology/28.1.75

Hauksson, E. (2000). Crustal structure and seismicity distribution adjacent to the Pacific and North America plate boundary in southern California. *Journal of Geophysical Research - Solid Earth*, *105*(B6), 13875–13903. https://doi.org/10.1029/2000JB900016

Haxel, G., & Dillon, J. (1978). The Pelona Orocopia Schist and Vincent–Chocolate Mountain thrust system, southern California. In D. G. Howell, & K. A. McDougall (Eds.), *Mesozoic Paleogeography of the Western United States*, *Pacific Section* (Vol. 2, pp. 453–469). Society of Economic Paleontologists and Mineralogists Pacific Coast Paleogeography Symposium.

Heermance, R. V., & Yule, D. (2017). Holocene slip rates along the San Andreas Fault System in the San Gorgonio Pass and implications for large earthquakes in southern California. *Geophysical Research Letters*, *44*, 5391–5400. https://doi.org/10.1002/2017GL072612

Howard, K. A., House, P. K., Dorsey, R. J., & Pearthree, P. A. (2015). River-evolution and tectonic implications of a major Pliocene aggradation on the lower Colorado River: the Bullhead Alluvium. *Geosphere*, *11*(1), 1–30. https://doi.org/10.1130/GES01059.1

Hubbard, J., Shaw, J. H., Dolan, J., Pratt, T. L., McAuliffe, L., & Rockwell, T. K. (2014). Structure and seismic hazard of the Ventura Avenue Anticline and Ventura Fault, California: Prospect for large, multisegment ruptures in the western Transverse Ranges. *Bulletin of the Seismological Society of America*, *104*(3), 1070–1087. https://doi.org/10.1785/0120130125

Ichinose, G., Day, S., Magistrale, H., Prush, T., Vernon, F., & Edelman, A. (1996). Crustal thickness variations beneath the Peninsular Ranges, southern California. *Geophysical Research Letters*, *23*(22), 3095–3098. https://doi.org/10.1029/96GL03020

Ingersoll, R. V., & Rumelhart, P. E. (1999). Three-stage evolution of the Los Angeles basin, southern California. *Geology*, *27*(7), 593–596. https://doi.org/10.1130/0091-7613(1999)027<0593:TSEOTL>2.3.CO;2

Jacobson, C. E., Grove, M., Pedrick, J. N., Barth, A. P., Marsaglia, K. M., Gehrels, G. E., & Nourse, J. A. (2011). Late Cretaceous–early Cenozoic tectonic evolution of the southern California margin inferred from provenance of trench and forearc sediments. *Geological Society of America Bulletin*, *123*(3-4), 485–506. https://doi.org/10.1130/B30238.1

Jennings, C. W., Strand, R. G., & Rogers, T. H. (1977). *Geologic map of California*. California Division of Mines and Geology. scale 1:750,000. Sacramento, CA: CaliforniaGeological Survey.

Jiang, H., & Lee, C.-T. A. (2017). Coupled magmatism–erosion in continental arcs: Reconstructing the history of the Cretaceous Peninsular Ranges batholith, southern California through detrital hornblende barometry in forearc sediments. *Earth and Planetary Science Letters*, *472*, 69–81. https://doi.org/10.1016/j.epsl.2017.05.009

Jordan, T. H. (1981). Global tectonic regionalization for seismological data analysis. *Bulletin of the Seismological Society of America*, *71*, 1131–1141.

Kaban, M. K., & Mooney, W. D. (2001). Density structure of the lithosphere in the southwestern United States and its tectonic significance. *Journal of Geophysical Research - Solid Earth*, *106*(B1), 721–739. https://doi.org/10.1029/2000JB900235

Kimbrough, D. L., Grove, M., & Morton, D. M. (2015). Timing and significance of gabbro emplacement within two distinct plutonic domains of the Peninsular Ranges batholith, southern and Baja California. *Geological Society of America Bulletin*, *127*(1-2), 19–37. https://doi.org/10.1130/B30914.1

Kistler, R. W., & Peterman, Z. E. (1978). *Reconstruction of crustal blocks of California on the basis of initial strontium isotopic compositions of Mesozoic granitic rocks*, *U.S. Geol. Surv. Prof. Paper 1071* (17 pp.). Washington, DC.

Kistler, R. W., Wooden, J. L., & Morton, D. M. (2003). Isotopes and ages in the northern Peninsular Ranges batholith, southern California. In *U.S. Geol. Sur. Open-File Report 03-489* (pp. 181–225). Washington, DC: United States Geological Survey.

Klotsko, S., Driscoll, N., Kent, G., & Brothers, D. (2015). Continental shelf morphology and stratigraphy offshore San Onofre, California: The interplay between rates of eustatic change and sediment supply. *Marine Geology*, *369*, 116–126. https://doi.org/10.1016/j.margeo.2015.08.003

Kohler, M. D., Magistrale, H., & Clayton, R. W. (2003). Mantle heterogeneities and the SCEC reference three-dimensional seismic velocity model version 3. *Bulletin of the Seismological Society of America*, *93*(2), 757–774. https://doi.org/10.1785/0120020017

Kucks, RP. (1999). Bouguer gravity anomaly data grid for the conterminous US, *U.S. Geological Survey Digital Data Series DDS-9*. Washington, DC: U.S. Geological Survey. https://mrdata.usgs.gov/services/gravity?request=getcapabilities&service=WMS&version=1.3

Lachenbruch, A. H., Sass, J. H., & Morgan, P. (1994). Thermal regime of the southern Basin and Range Province: 2. Implications of heat flow for regional extension and metamorphic core complexes. *Journal of Geophysical Research - Solid Earth*, *99*(B11), 22,121–22,133. https://doi.org/10.1029/94JB01890

Langenheim, V. E., Jachens, R. C., Matti, J. C., Hauksson, E., Morton, D. M., & Christensen, A. (2005). Geophysical evidence for wedging in the San Gorgonio Pass structural knot, southern San Andreas fault zone, southern California. *Geological Society of America Bulletin*, *117*(11), 1554–1572. https://doi.org/10.1130/B25760.1

Langenheim, V. E., Jachens, R. C., Morton, D. M., Kistler, R. W., & Matti, J. C. (2004). Geophysical and isotopic mapping of preexisting crustal structures that influenced the location and development of the San Jacinto fault zone, southern California. *Geological Society of America Bulletin*, *116*(9), 1143–1157. https://doi.org/10.1130/B25277.1

Langenheim, V. E., Lee, T.-C., Biehler, S., Jachens, R. C., & Morton, D. M. (2006). *Isostatic gravity map with geology of the Santa Ana 30' x 60' quadrangle, Southern California*, *Sci. Invest. Map 2951, U. S. Geol. Surv.* (25 pp.). Washington, DC: U.S. Geological Survey.

Lee, E.-J., & Chen, P. (2016). Improved basin structures in Southern California obtained through full-3D seismic waveform tomography (F3DT). *Seismological Research Letters*, *87*(4), 874–881. https://doi.org/10.1785/0220160013

Lee, E.-J., & Chen, P. (2017). Subsurface fault geometries in Southern California illuminated through full-3D seismic waveform tomography (F3DT). *Tectonophysics*, *703-704*, 42–49. https://doi.org/10.1016/j.tecto.2017.03.005

Lee, E.-J., Chen, P., & Jordan, T. H. (2014). Testing waveform predictions of 3D velocity models against two recent Los Angeles earthquakes. *Seismological Research Letters*, *85*(6), 1275–1284. https://doi.org/10.1785/0220140093

Lee, E.-J., Chen, P., Jordan, T. H., Maechling, P. B., Denolle, M. A. M., & Beroza, G. C. (2014). Full-3D tomography for crustal structure in Southern California based on the scattering-integral and the adjoint-wavefield methods. *Journal of Geophysical Research: Solid Earth*. *119*, 6421–6451. https://doi.org/10.1002/2014JB011346

Lekić, V., & Romanowicz, B. (2011a). Tectonic regionalization without a priori information: A cluster analysis of upper mantle tomography. *Earth and Planetary Science Letters*, *308*(1-2), 151–160. https://doi.org/10.1016/j.epsl.2011.05.050

Lekić, V., & Romanowicz, B. (2011b). Inferring upper-mantle structure by full waveform tomography with the spectral element method. *Geophysical Journal International*, *185*(2), 799–831. https://doi.org/10.1111/j.1365-246X.2011.04969.x

Lewis, J. L., Day, S. M., Magistrale, H., Eakins, J., & Vernon, F. (2000). Regional crustal thickness variations of the Peninsular Ranges, southern California. *Geology*, *28*(4), 303. https://doi.org/10.1130/0091-7613(2000)28<303:RCTVOT>2.0.CO;2

Lin, G., Thurber, C. H., Zhang, H., Hauksson, E., Shearer, P. M., Waldhauser, F., et al. (2010). A California statewide three-dimensional seismic velocity model from both absolute and differential times. *Bulletin of the Seismological Society of America*, *100*(1), 225–240. https://doi.org/10.1785/0120090028

Lloyd, S. P. (1982). Least squares quantization in pcm. *IEEE Transactions on Information Theory*, *28*(2), 129–137. https://doi.org/10.1109/TIT.1982.1056489

Lutter, W. J., Fuis, G. S., Ryberg, T., Okaya, D. A., Clayton, R. W., Davis, P. M., et al. (2004). Upper crustal structure from the Santa Monica mountains to the Sierra Nevada, southern California: Tomographic results from the Los Angeles regional seismic experiment, phase II (LARSE II). *Bulletin of the Seismological Society of America*, *94*(2), 619–632. https://doi.org/10.1785/0120030058

Lutter, W. J., Fuis, G. S., Thurber, C. H., & Murphy, J. (1999). Tomographic images of the upper crust from the Los Angeles basin to the Mojave Desert, California: Results from the Los Angeles region seismic experiment. *Journal of Geophysical Research - Solid Earth*, *104*(B11), 25,543–25,565. https://doi.org/10.1029/1999JB900188

Lyakhovsky, V., & Ben-Zion, Y. (2009). Evolving geometrical and material properties of fault zones in a damage rheology model. *Geochemistry, Geophysics, Geosystems*, *10*, Q11011. https://doi.org/10.1029/2009GC002543

MacQueen, J. (1967). Some methods for classification and analysis of multivariate observations. In *Proceedings of the fifth Berkeley symposium on mathematical statistics and probability* (Vol. 1, pp. 281–297). Berkeley and Los Angeles, CA: University of California Press.

Magistrale, H., Day, S., Clayton, R. W., & Graves, R. (2000). The SCEC southern California reference three-dimensional seismic velocity model version 2. *Bulletin of the Seismological Society of America*, *90*(6B), S65–S76. https://doi.org/10.1785/0120000510

Magistrale, H., & Zhou, H. (1996). Lithologic control of the depth of earthquakes in southern California. *Science*, *273*(5275), 639–642. https://doi.org/10.1126/science.273.5275.639

Malin, P. E., Goodman, E. D., Henyey, T. L., Li, Y. G., Okaya, D. A., & Saleeby, J. B. (1995). Significance of seismic reflections beneath a tilted exposure of deep continental-crust, Tehachapi Mountains, California. *Journal of Geophysical Research - Solid Earth*, *100*(B2), 2069–2087. https://doi.org/10.1029/94JB02127

Marshall, S. T., Funning, G. J., Krueger, H. E., Owen, S. E., & Loveless, J. P. (2017). Mechanical models favor a ramp geometry for the Ventura-Pitas Point fault, California. *Geophysical Research Letters*, *44*, 1311–1319. https://doi.org/10.1002/2016GL072289

Mason, C. C., Spotila, J. A., Axen, G., Dorsey, R. J., Luther, A., & Stockli, D. F. (2017). Two-phase exhumation of the Santa Rosa Mountains: Low- and high-angle normal faulting during initiation and evolution of the southern San Andreas Fault system. *Tectonics*, *36*, 2863–2881. https://doi.org/10.1002/2017TC004498

McCaffree Pellerin, C. L., & Christensen, N. I. (1998). Interpretation of crustal seismic velocities in the San Gabriel-Mojave region, southern California. *Tectonophysics*, *286*(1-4), 253–271. https://doi.org/10.1016/S0040-1951(97)00269-2

McQuarrie, N., & Wernicke, B. P. (2005). An animated tectonic reconstruction of southwestern North America since 36 Ma. *Geosphere*, *1*(3), 147–172. https://doi.org/10.1130/GES00016.1

Meisling, K. E., & Weldon, R. J. (1989). Late Cenozoic tectonics of the northwestern San Bernardino Mountains, southern California. *Geological Society of America Bulletin*, *101*(1), 106–128. https://doi.org/10.1130/0016-7606(1989)101<0106:LCTOTN>2.3.CO;2

Miller, J. S., Glazner, A. F., Farmer, G. L., Suayah, I. B., & Keith, L. A. (2000). A Sr, Nd, and Pb isotopic study of mantle domains and crustal structure from Miocene volcanic rocks in the Mojave Desert, California. *Geological Society of America Bulletin*, *112*(8), 1264–1279. https://doi.org/10.1130/0016-7606(2000)112<1264:ASNAPI>2.0.CO;2

Mooney, W. D., Laske, G., & Masters, T. G. (1998). CRUST 5.1: A global crustal model at 5° x 5°. *Journal of Geophysical Research - Solid Earth*, *103*(B1), 727–747. https://doi.org/10.1029/97JB02122

Nadin, E. S., & Saleeby, J. B. (2008). *Disruption of regional primary structure of the Sierra Nevada Batholith by the Kern Canyon fault system, California*, *Geol. Soc. Am. Special Paper* (Vol. 438, pp. 429–454). Boulder CO: Geological Society of America.

Norton, I. (2011). Two-stage formation of Death Valley. *Geosphere*, *7*(1), 171–182. https://doi.org/10.1130/GES00588.1

Ozakin, Y., & Ben-Zion, Y. (2015). Systematic receiver function analysis of the Moho geometry in the Southern California plate-boundary region. *Pure and Applied Geophysics*, *172*(5), 1167–1184. https://doi.org/10.1007/s00024-014-0924-6

Page, B. M. (1970). Sur-Nacimiento Fault Zone of California: Continental margin tectonics. *Geological Society of America Bulletin*, *81*(3), 667–690. https://doi.org/10.1130/0016-7606(1970)81[667:SFZOCC]2.0.CO;2

Persaud, P., Ma, Y., Stock, J. M., Hole, J. A., Fuis, G. S., & Han, L. (2016). Fault zone characteristics and basin complexity in the southern Salton Trough, California. *Geology*, *44*(9), 747–750. https://doi.org/10.1130/G38033.1

Platt, J. P., Behr, W. M., & Cooper, F. J. (2015). Metamorphic core complexes: windows into the mechanics and rheology of the crust. *Journal of the Geological Society*, *172*(1), 9–27. https://doi.org/10.1144/jgs2014-036

Porter, R., Zandt, G., & McQuarrie, N. (2011). Pervasive lower-crustal seismic anisotropy in Southern California: Evidence for underplated schists and active tectonics. *Lithosphere*, *3*(3), 201–220. https://doi.org/10.1130/L126.1

Rey, P., Vanderhaeghe, O., & Teyssier, C. (2001). Gravitational collapse of the continental crust: definition, regimes and modes. *Tectonophysics*, *342*(3-4), 435–449. https://doi.org/10.1016/S0040-1951(01)00174-3

Richards-Dinger, K. B., & Shearer, P. M. (1997). Estimating crustal thickness in southern California bv stacking *PmP* arrivals. *Journal of Geophysical Research - Solid Earth*, *102*(B7), 15,211–15,224. https://doi.org/10.1029/97JB00883

Roberts, C. W., & Jachens, R. C. (1999). Preliminary aeromagnetic anomaly map of California. In *U. S. Geological Survey Open-File Report 99-440* (pp. 14). Washington DC: U. S. Geological Survey. https://doi.org/10.3133/ofr99440

Rockwell, T. (1988). Neotectonics of the San Cayetano fault, Transverse Ranges, California. *Geological Society of America Bulletin*, *100*(4), 500–513. https://doi.org/10.1130/0016-7606(1988)100<0500:NOTSCF>2.3.CO;2

Ryberg, T., & Fuis, G. S. (1998). The San Gabriel Mountains bright reflective zone: Possible evidence of young mid-crustal thrust faulting in southern California. *Tectonophysics*, *286*(1-4), 31–46. https://doi.org/10.1016/S0040-1951(97)00253-9

Saleeby, J. (2003). Segmentation of the Laramide slab—Evidence from the southern Sierra Nevada region. *Geological Society of America Bulletin*, *115*, 655–668. https://doi.org/10.1130/0016-7606(2003)115<0655:SOTLSF>2.0.CO;2

Saleeby, J. (2011). Geochemical mapping of the Kings-Kaweah ophiolite belt, California—Evidence for progressive mélange formation in a large offset transform-subduction initiation environment. In J. Wakabayashi, & Y. Dilek (Eds.), *Mélanges: Processes of Formation and Societal Significance*, *Geol. Soc. Am. Special Paper* (Vol. 480, pp. 31–73). Boulder, CO: Geological Society of America. https://doi.org/10.1130/2011.2480(02)

Saleeby, J., Farley, K. A., Kistler, R. W., Fleck (2007). Thermal evolution and exhumation of deep-level batholithic exposures, southernmost Sierra Nevada, *California Geological Society of America Special Papers*, *419*, 39.

Saleeby, J., Le Pourhiet, L., Saleeby, Z., & Gurnis, M. (2012). Epeirogenic transients related to mantle lithosphere removal in the southern Sierra Nevada region, California, part I: Implications of thermomechanical modeling. *Geosphere*, *8*(6), 1286–1309. https://doi.org/10.1130/GES00746.1

Sass, J. H., Lachenbruch, A. H., Galanis, S. P. Jr., Morgan, P., Priest, S. S., Moses, T. H. Jr., & Munroe, R. J. (1994). Thermal regime of the southern Basin and Range Province: 1. Heat flow data from Arizona and the Mojave Desert of California and Nevada. *Journal of Geophysical Research - Solid Earth*, *99*(B11), 22,093–22,119. https://doi.org/10.1029/94JB01891

Sharman, G. R., Graham, S. A., Grove, M., Kimbrogh, D. L., & Wright, J. E. (2015). Detrital zircon provenance of the Late Cretaceous–Eocene California forearc: influence of Laramide low-angle subduction on sediment dispersal and paleogeography. *Geological Society of America Bulletin*, *127*(1-2), 38–60. https://doi.org/10.1130/B31065.1

Shaw, J. H., Plesch, A., Tape, C., Suess, M. P., Jordan, T. H., Ely, G., et al. (2015). Unified structural representation of the Southern California crust and upper mantle. *Earth and Planetary Science Letters*, *415*, 1–15. https://doi.org/10.1016/j.epsl.2015.01.016

Silver, L. T., Taylor, H. P., & Chappell, B. W. (1979). Some petrological, geochemical and geochronological observations the Peninsula Ranges batholith near the international border of the U.S.A. and Mexico. In P. L. Abbott, & V. R. Todd (Eds.), *Mesozoic Crystalline Rocks: Peninsular Ranges Batholith and Pegmatites, Point Sal Ophiolite* (pp. 83–110). San Diego, Calif: San Diego State University.

Simpson, R. W., Jachens, R. C., Blakely, R. J., & Saltus, R. W. (1986). A new isostatic residual gravity map of the conterminous United States with a discussion on the significance of isostatic residual anomalies. *Journal of Geophysical Research - Solid Earth*, *91*(B8), 8348–8372. https://doi.org/10.1029/JB091iB08p08348

Spotila, J. A., Farley, K. A., & Sieh, K. (1998). Uplift and erosion of the San Bernardino Mountains associated with transpression along the San Andreas fault, California, as constrained by radiogenic helium thermochronometry. *Tectonics*, *17*(3), 360–378. https://doi.org/10.1029/98TC00378

Spotila, J. A., & Sieh, K. (2000). Architecture of transpressional thrust faulting in the San Bernardino Mountains, southern California, from deformation of a deeply weathered surface. *Tectonics*, *19*(4), 589–615. https://doi.org/10.1029/1999TC001150

Stevens, C. H., & Stone, P. (2005). Interpretation of the Last Chance thrust, Death Valley region, California, as an Early Permian décollement in a previously undeformed shale basin. *Earth-Science Reviews*, *73*(1-4), 79–101. https://doi.org/10.1016/j.earscirev.2005.04.005

Süss, M. P., & Shaw, J. H. (2003). P wave seismic velocity structure derived from sonic logs and industry reflection data in the Los Angeles basin, California. *Journal of Geophysical Research - Solid Earth*, *108*(B3), 2170. https://doi.org/10.1029/2001JB001628

Taborda, R., Azizzadeh-Roodpish, S., Khoshnevis, N., & Cheng, K. (2016). Evaluation of the southern California seismic velocity models through simulation of recorded events. *Geophysical Journal International*, *205*(3), 1342–1364. https://doi.org/10.1093/gji/ggw085

Tape, C., Liu, Q., Maggi, A., & Tromp, J. (2010). Seismic tomography of the southern California crust based on spectral-element and adjoint methods. *Geophysical Journal International*, *180*(1), 433–462. https://doi.org/10.1111/j.1365-246X.2009.04429.x

Tape, C., Plesch, A., Shaw, J. H., & Gilbert, H. (2012). Estimating a continuous Moho surface for the California unified velocity model. *Seismological Research Letters*, *83*, 728–735.

Tosdal, R. M., & Wooden, J. L. (2015). Construction of the Jurassic magmatic arc, southeast California and southwest Arizona. In T. H. Anderson, A. N. Didenko, C. L. Johnson, A. I. Khanchuk, & J. H. MacDonald, Jr. (Eds.), *Late Jurassic Margin of Laurasia—A Record of Faulting Accommodating Plate Rotation*, *Geol. Soc. Am. Special Paper* (Vol. 513, pp. 189–221). Boulder CO: Geological Society of America. https://doi.org/10.1130/2015.2513(04)

Wernicke, B., & Axen, G. J. (1988). On the role of isostasy in the evolution of normal fault systems. *Geology*, *16*(9), 848–851. https://doi.org/10.1130/0091-7613(1988)016<0848:OTROII>2.3.CO;2

Whitmeyer, S. J., & Karlstrom, K. E. (2007). Tectonic model for the Proterozoic growth of North America. *Geosphere*, *3*(4), 220–259. https://doi.org/10.1130/GES00055.1

Xia, H., & Platt, J. P. (2018). Is the Vincent fault in southern California the Laramide subduction zone megathrust? *Geological Society of America Bulletin*, *131*(1-2), 120–136. https://doi.org/10.1130/B31870.1

Yan, Z., & Clayton, R. W. (2007). Regional mapping of the crustal structure in southern California from receiver functions. *Journal of Geophysical Research - Solid Earth*, *112*(B5), B05311. https://doi.org/10.1029/2006JB004622

Yule, D. (2009). The enigmatic San Gorgonio Pass. *Geology*, *37*(2), 191–192. https://doi.org/10.1130/focus022009.1

Zhu, L. (2000). Crustal structure across the San Andreas Fault, southern California from teleseismic converted waves. *Earth and Planetary Science Letters*, *179*(1), 183–190. https://doi.org/10.1016/S0012-821X(00)00101-1

Zhu, L., & Kanamori, H. (2000). Moho depth variation in southern California from teleseismic receiver functions. *Journal of Geophysical Research - Solid Earth*, *105*(B2), 2969–2980. https://doi.org/10.1029/1999JB900322

Zigone, D., Ben-Zion, Y., Campillo, M., & Roux, P. (2015). Seismic tomography of the Southern California plate boundary region from noise-based Rayleigh and Love waves. *Pure and Applied Geophysics*, *172*(5), 1007–1032. https://doi.org/10.1007/s00024-014-0872-1